J. Fluid Mech. (1987), *vol.* 176, *pp.* 33–66
Printed in Great Britain

The structure of the vorticity field in homogeneous turbulent flows

By MICHAEL M. ROGERS†
Stanford University, Stanford, CA 94305, USA

AND PARVIZ MOIN‡
NASA Ames Research Center, Moffett Field, CA 94035, USA

(Received 12 November 1985)

The structure of the vorticity fields in homogeneous turbulent shear flow and various irrotational straining flows is examined using results from direct numerical simulations of the unsteady, incompressible Navier–Stokes equations with up to $128 \times 128 \times 128$ grid points. In homogeneous shear flow, the distribution of the inclination angle of the vorticity vectors and contour plots of two-point correlations of both velocity and vorticity are consistent with the existence of persistent vortical structures inclined with respect to the flow direction. Early in the development of these shear flows, the angle of inclination at which most of these structures are found is near 45°; after the flow develops, this angle lies between 35°–40°. Instantaneous vorticity-vector and vortex-line plots confirm the presence of hairpin vortices in this flow at the two Reynolds numbers simulated. These vortices are formed by the roll-up of sheets of mean spanwise vorticity. The average hairpin leg spacing decreases with increasing Reynolds number but increases relative to the Taylor microscale for developed shear flows. Examination of irrotational axisymmetric contraction, axisymmetric expansion, and plane strain flows shows, as expected, that the vorticity tends to be aligned with the direction of positive strain. For example, the axisymmetric contraction flow is dominated by coherent longitudinal vortices. Without the presence of mean shear, however, hairpin structures do not develop. The simulations strongly indicate that the vorticity occurs in coherent filaments that are stretched and strengthened by the mean strain. When compressed, these filaments appear to buckle rather than to decrease in strength.

1. Introduction

Recently, there has been much effort devoted to the search for and examination of organized structures in turbulent flows. Virtually all the work in this area has concentrated on inhomogeneous flows such as the turbulent boundary layer or the mixing layer. A notable exception is the work of Townsend (1970), who proposes a 'double-roller eddy', or a pair of inclined vortices, as the characteristic structure in both homogeneous and inhomogeneous shear flows.

Beginning with Theodorsen (1952), the existence of hairpin vortices in turbulent boundary layers has been conjectured by a number of investigators. Flow visualization by Head & Bandyopadhyay (1981) provided support for the presence of hairpin vortices in turbulent boundary layers. Recently, using numerically simulated flow

† Present address: NASA Ames Research Center, Moffet Field, CA 94035, USA.
‡ Also Department of Mechanical Engineering, Stanford University, Stanford, CA 94305, USA.

fields, Moin & Kim (1985) showed that fully developed turbulent channel flow is dominated by hairpin vortices, often inclined at 45° to the mean-flow direction. Their conclusion was based on examination of the probability distribution of the inclination angle of the vorticity vectors, two-point velocity and vorticity correlations with various directions of 'probe' separation, plots of vorticity vectors projected onto inclined planes, and the topology of vortex lines traced in three-dimensional space. Kim & Moin (1986) used conditional-sampling techniques to verify that the bursting process is associated with the hairpin vortices.

In the Moin & Kim study, it was apparent that hairpin vortices are often formed by the roll-up of sheets of spanwise (mean) vorticity in the regions away from the walls. This observation, and the fact that deformation of sheets of spanwise vorticity by random velocity fluctuations and stretching by the mean rate of strain are sufficient ingredients for the generation of the hairpins, led us to conjecture that hairpin vortices are the characteristic structures not only in wall-bounded shear flows but in *all* turbulent shear flows. To validate this conjecture, we applied the same techniques used in the channel-flow study to the simplest turbulent shear flow, homogeneous turbulence in the presence of uniform shear.

In addition, homogeneous turbulent flows subject to various uniform irrotational strains were examined for persistent organized structure. These studies indicate that mean shear is required for the generation of hairpins.

The objective of this investigation is to examine a number of homogeneous 'building-block' flows to determine if their organized structure, if any exists, is similar to that found in inhomogeneous flows. Such similarities would reinforce the relevance of these flows to the understanding of more complex turbulent flows.

In §2, the numerical method used to generate the flow data is briefly presented, along with the dimensionless parameters of the computed fields. An analysis of statistical correlations and instantaneous vorticity fields is used in §§3 and 4 to ascertain whether organized structure exists in the flow fields; §3 covers shear flow at two Reynolds numbers and §4 covers three forms of irrotationally strained flows. A summary of results and conclusions is presented in §5.

2. Numerical simulation of homogeneous turbulent flows

All the flow fields examined in this report were generated by direct numerical simulation of the three-dimensional, time-dependent, incompressible Navier–Stokes and continuity equations. These calculations were performed by using Rogallo's (1981) computer code with up to $128 \times 128 \times 128$ grid points. Fourier-spectral methods are used for the spatial representation of the velocity field. The initial velocity fields were divergence-free and random, and had a prescribed three-dimensional energy spectrum. The computational grid deformed to follow the mean flow, permitting the application of periodic boundary conditions. Throughout this paper we refer to u (or u_1), v (or u_2) and w (or u_3) as the fluctuating velocity components in the x-, y- and z-directions respectively. U_1 (or simply U), U_2 and U_3 are the corresponding mean-velocity components. Similarly, ω_x (or ω_1), ω_y (or ω_2) and ω_z (or ω_3) are the components of fluctuating vorticity in the same three directions. For the shear-flow cases it is convenient to define two additional directions, the s- and n-directions, which correspond to the x- and y-directions rotated counterclockwise by 45°. The s-direction corresponds to the direction of principal elongation and the n-direction is the direction of principal contraction. The fluctuating components of vorticity along these directions are referred to as ω_s and ω_n.

2.1. *Homogeneous turbulent shear flow*

The homogeneous-shear-flow results presented in this paper are taken from a low-Reynolds-number simulation (§3.1) on a $128 \times 64 \times 64$ grid, and a higher-Reynolds-number simulation (§3.2) on a $128 \times 128 \times 128$ grid. The grid spacing for the low-Reynolds-number case was 1.46 when non-dimensionalized by $(\nu/S)^{\frac{1}{2}}$, where S is the shear rate and ν the kinematic viscosity. The grid spacing for the high-Reynolds-number case was twice as long in the streamwise direction as in the other two coordinate directions with $\Delta x/(\nu/S)^{\frac{1}{2}} = 4.14$. The imposed mean flow is in the x-direction and is a linear function of y:

$$U(y) = Sy.$$

The transformation that moves the computational grid with the mean flow is thus given by

$$x' = x - Syt, \quad y' = y, \quad z' = z, \quad t' = t.$$

As a result of the imposed mean shear, the computational grid becomes skewed as time increases. The mean shear moves (x, z)-planes at large y further than those at small y. To allow the simulation to progress for a substantial time, it is necessary to remesh the grid at regular intervals. The remeshing procedure utilizes the periodic boundary condition in the streamwise direction to move data from the skewed grid onto a grid skewed in the opposite sense. After remeshing, the grid progresses to its initial orthogonal position and eventually continues to the skewed position where remeshing becomes necessary again. On the computational grids used here, remeshing is done at St of $1.0, 3.0, 5.0, \ldots$ to avoid having to interpolate data onto the new grid. The fields at St of $0, 2.0, 4.0, \ldots$ are on an orthogonal mesh and are saved for analysis. For the low-Reynolds-number case, $S = 10.0$ and $\nu = 0.045$. In the high-Reynolds-number case, $S = 28.3$ and $\nu = 0.010$. The values of S and ν are in arbitrary units; however, they can be used to form non-dimensional length ($l^+ = l/(\nu/S)^{\frac{1}{2}}$) and time ($t = St$) scales. The total dimensionless integration time for the low-Reynolds-number calculation was $St = 4.0$, beyond which time the shearing created structures approaching the size of the computational box. We examined the field at $St = 2.0$, which had microscale Reynolds number $Re_\lambda = 14.2$ (based on $q = (\overline{u_i u_i})^{\frac{1}{2}}$ and longitudinal Taylor microscale $\lambda_{11,1}$). The high-Reynolds-number simulation did not outgrow the computational box size until about $St = 16.0$. Even this highest Reynolds number field at $St = 16.0$ does not have a distinct inertial subrange and the small scales, although more isotropic than the energy-containing eddies, retain a fair degree of anisotropy. We chose to examine in detail the field at $St = 8.0$, which had the best resolution of the Kolmogorov lengthscale (minimizing the amount of high-wavenumber vorticity which might conceal large-scale vortex structure) and had developed long enough to be well into the asymptotic region of growing turbulence kinetic energy and lengthscales. For this field $Re_\lambda = 72.6$. The flow cannot reach a statistically steady state with the length and velocity scales continually increasing but it does seem to be approaching structural equilibrium with the anisotropy levels apparently asymptoting to constant values. The higher-Reynolds-number case is near one of the cases computed by Rogallo (BSH10: $Re_\lambda = 56.7$ at $St = 8.0$), and its asymptotic flow statistics are in good agreement with the data of Tavoularis & Corrsin (1981). For example, figure 1 shows the history of the turbulent intensities from the present calculation and from the experimental data. Table 1 compares non-dimensional parameters obtained in these runs with experimental results. Note that at $St = 8.6$ the experimental microscale Reynolds number is 284. Although the

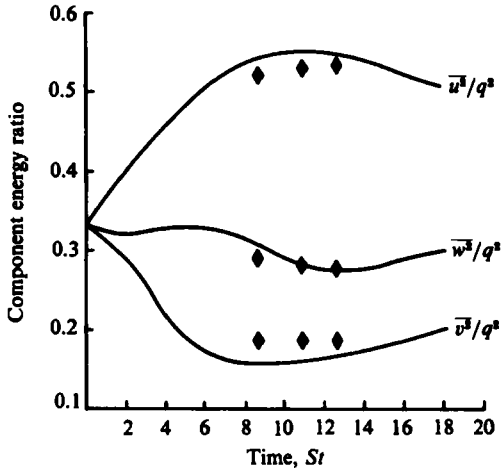

FIGURE 1. History of the component energy ratios of homogeneous turbulent shear flow. Symbols are from data of Tavoularis & Corrsin (1981), and the solid lines are the computational results.

	low Re_λ $St = 2.0$	high Re_λ $St = 8.0$	TC $St = 8.6$	TC $St = 12.7$	HGC $St = 11.9$	CHC $St = 3.3$
$Re_\lambda = q\lambda_{11,1}/\nu$	14.2	72.6	284	364	300	180
$Re_L = qL_{11,1}/\nu$	22.2	118	2100	3600	2800	1100
$Re_T = q^4/\epsilon\nu$	26.1	391	9900	15000	13000	3200
$SL_{11,1}/q$	2.66	2.60	2.8	2.8	2.3	2.0
Sq^2/ϵ	3.14	8.65	13	12	11	5.8
$\overline{u_1^2}/q^2$	0.43	0.53	0.52	0.53	0.50	0.47
$\overline{u_2^2}/q^2$	0.26	0.16	0.19	0.19	0.20	0.25
$\overline{u_3^2}/q^2$	0.31	0.31	0.29	0.28	0.30	0.28
$\overline{u_1 u_2}/u_1' u_2'$	0.55	0.57	0.45	0.45	0.47	0.50
σ_1/σ_2	3.8	6.2	4.2	4.3	4.1	2.3
σ_1/σ_3	1.7	1.9	2.0	2.1	1.9	—
α	−33°	−21°	−20°	−20°	−22.3°	−28°

TABLE 1. Comparison of shear simulations with experiments. TC, Tavoularis & Corrsin (1981); HGC, Harris, Graham & Corrsin (1977); CHC, Champagne, Harris & Corrsin (1970); $L_{11,1}$, integral lengthscale from R_{uu} correlation in x-direction; $\epsilon = \nu\overline{(\partial u_i/\partial x_j)(\partial u_i/\partial x_j)}$ = dissipation; $u_1' = (\overline{u_1^2})^{\frac{1}{2}}$, $u_2' = (\overline{u_2^2})^{\frac{1}{2}}$; $\sigma_1/\sigma_2, \sigma_1/\sigma_3$, ratio of principal stresses; α, angle of principal axes; other quantities defined in the text.

low-Reynolds-number simulation has not reached an asymptotic state, its flow statistics are remarkably near the experimental data of Champagne, Harris & Corrsin (1970) at $St = 3.3$. In both the simulations and the experiments, the ratios of the principal stresses, σ_1/σ_2 and σ_1/σ_3, decrease and the angle of the principal axes α increases as Reynolds number decreases. The principal stresses of the velocity field are defined by

$$\sigma_{1,2} = -\tfrac{1}{2}(\overline{u_1^2}+\overline{u_2^2}) \mp [\tfrac{1}{2}(\overline{u_1^2}-\overline{u_2^2})^2 + (\overline{u_1 u_2})^2]^{\frac{1}{2}},$$

$$\sigma_3 = \overline{u_3^2},$$

and the angle of the principal axes of the Reynolds stress tensor is

$$\alpha = \tfrac{1}{2}\tan^{-1}\left(\frac{2\overline{u_1 u_2}}{\overline{u_1^2}-\overline{u_2^2}}\right).$$

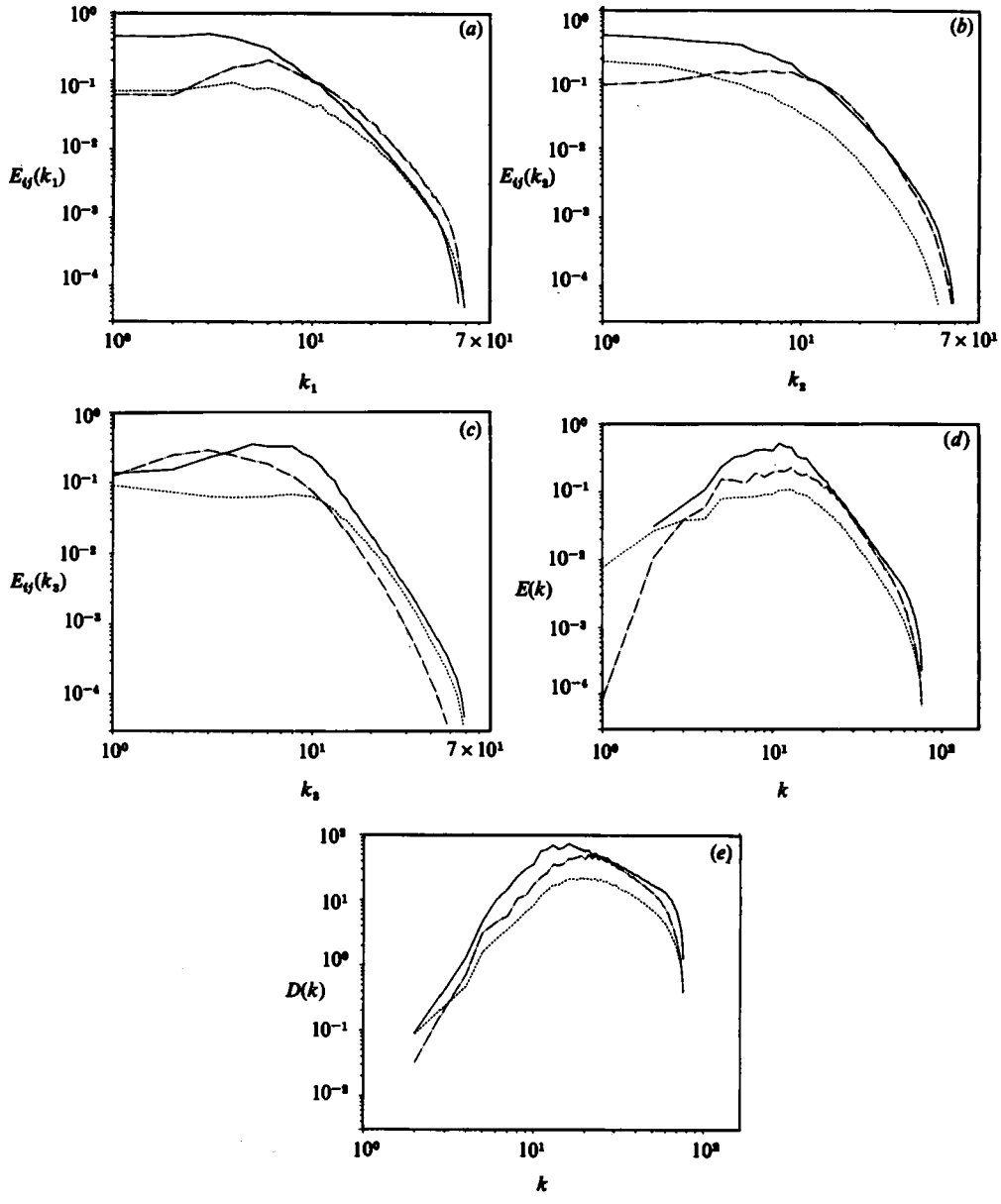

FIGURE 2. Spectra from the high-Reynolds-number simulation at $St = 8.0$. ——, uu-spectra; – – – –, vv-spectra; —·—, ww-spectra; (*a*) one-dimensional energy spectra as a function of k_1; (*b*) one-dimensional energy spectra as a function of k_2; (*c*) one-dimensional energy spectra as a function of k_3; (*d*) three-dimensional energy spectra; (*e*) three-dimensional dissipation spectra.

For a detailed comparison of these and other quantities with the data for a variety of flow parameters, see Rogallo (1981). Both energy and dissipation spectra were computed to ensure that the mesh adequately resolved all important lengthscales. The spectra for the high-Reynolds-number shear case are shown in figure 2. The three-dimensional dissipation spectrum $D(k)$ is obtained from $D(k) = k^2E(k)$, where $E(k)$ is the three-dimensional energy spectrum and k is the magnitude of the wavenumber vector. It was necessary to adequately represent the dissipation spectra

since we were particularly interested in the structure of the vorticity fields. The sharp drop at the high-wavenumber end of the dissipation spectra is due to the limited number of points in spherical shells in wave space with a high wavenumber magnitude. The low-Reynolds-number calculation was carried out to provide very good resolution of small dissipative scales and to prevent a wide range of scales from concealing possible organized structure. The ratios of the mesh size to the Kolmogorov lengthscale of the low- and high-Reynolds-number cases are 1.87 (at $St = 2.0$) and 3.95 (at $St = 8.0$) respectively; thus the low-Reynolds-number case has better resolution of the small scales. Since the Kolmogorov scale is not known prior to generating a numerical solution, it is useful to note that the length $(\nu/S)^{\frac{1}{2}}$ is a reasonable estimate of the size of small-scale structures, at least over the range of S and ν used in our simulations. This is related to the diameter of the Burgers (1948) vortex

$$l = \left(\frac{2\nu}{A}\right)^{\frac{1}{2}},$$

where A is the strain rate. The scale l is a measure of the equilibrium diameter of a vortex subjected to uniform stretching along its axis in a viscous fluid.

2.2. *Homogeneous irrotational straining flows*

Several homogeneous irrotational straining flows were examined. The flow fields were generated by Lee & Reynolds (1985) on a $128 \times 128 \times 128$ grid that deformed with the mean strain, and were computed at low Reynolds numbers to clearly reveal vortical structure. All simulations were begun from an isotropic field that had been allowed to develop a realistic energy spectrum. One field each of axisymmetric contraction, axisymmetric expansion and plane strain was selected for this study. The non-dimensional strain rate Sq^2/ϵ ranged from 3.09 to 3.81, where

$$S = (2S_{ij}S_{ij})^{\frac{1}{2}}, \quad S_{ij} = \frac{1}{2}\left(\frac{\partial U_i}{\partial x_j} + \frac{\partial U_j}{\partial x_i}\right),$$

$$\epsilon = \nu\overline{\left(\frac{\partial u_i}{\partial x_j}\frac{\partial u_i}{\partial x_j}\right)}.$$

This definition of S is consistent with the definition used in the shear cases. The fields were selected to have significant contribution by the nonlinear terms of the Navier–Stokes equations. For high strain rates, $Sq^2/\epsilon > 10$, the flows behaved in accordance with rapid-distortion theory; the structures observed were simply those of the initial conditions stretched by the mean strain, and anisotropy levels showed little increase with further increase in non-dimensional strain rate. The ratios of the mesh sizes to the Kolmogorov lengthscales are 1.44, 1.25 and 1.11 for the contraction, expansion and plane-strain cases respectively. Table 2 shows the parameters of the selected fields and the coordinates in which the strain was imposed. In this table the total strain is defined by

$$\text{total strain} = \exp \int S(t')\,dt'.$$

For a comparison of typical runs with experimental results, see Rogallo (1981).

	Axisymmetric contraction	Axisymmetric expansion	Plane strain
Total strain	3.32	3.32	4.00
$Re_\lambda = q\lambda_{11,1}/\nu$	17.2	15.9	13.1
$Re_L = qL_{11,1}/\nu$	19.2	28.2	16.6
$Re_T = q^4/\epsilon\nu$	48.1	48.0	41.6
$SL_{11,1}/q$	1.29	1.82	1.52
Sq^2/ϵ	3.22	3.09	3.81
$\overline{u_1^2}/q^2$	0.150	0.525	0.335
$\overline{u_2^2}/q^2$	0.412	0.241	0.506
$\overline{u_3^2}/q^2$	0.438	0.234	0.159

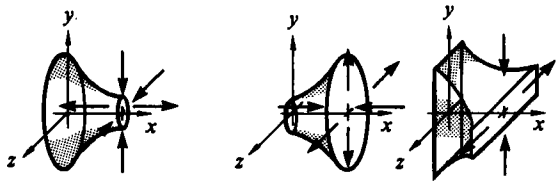

TABLE 2. The parameters of the fields selected for study, and the coordinates in which the strain was imposed. Total strain = $\exp\int S(t')\,dt'$.

3. Structure of the vorticity fields in the homogeneous-shear-flow simulations

The computed flow fields were analysed in a manner similar to the channel-flow study of Moin & Kim (1985). Since the low-Reynolds-number case has a limited range of scales, it is easier to identify the organized structures in this flow. For this reason we will examine this case first and then analyse the high-Reynolds-number field.

3.1. *Low-Reynolds-number shear case*

At each grid point, the inclination angle of the vorticity vector to the mean-flow direction

$$\theta = \tan^{-1}(\omega_y/\omega_x)$$

is calculated. The sign convention for the angle θ and the coordinate system are shown in figure 3. Figure 4 shows the distribution of this angle at $St = 2.0$. The contribution from each grid point to the histogram is weighted by the magnitude of the projection of the corresponding vorticity vector onto (x, y)-planes, $(\omega_x^2+\omega_y^2)^{\frac{1}{2}}$. The distribution attains rather sharp maxima at 45° and −135° (the direction of principal elongation of the mean strain) with a maximum-to-minimum ratio of about 20:1. When the contributions to the histogram are not weighted by the vorticity magnitude, the maximum-to-minimum ratio decreases to approximately 5:1. Figure 5 shows the weighted distribution of θ for the initial flow field (i.e. $St = 0$). The initial vorticity field exhibits no directional preference as expected for an isotropic field. Apparently, the shearing motion causes the remarkable organization of the instantaneous vorticity vectors displayed in figure 4. The fact that the weighted histogram has a substantially higher maximum-to-minimum ratio than the unweighted histogram indicates that not only are the vorticity vectors predominantly oriented at 45° or −135°, but also that such orientation is accompanied by increased vorticity magnitude. This is as expected because a vortex filament so oriented is subject to

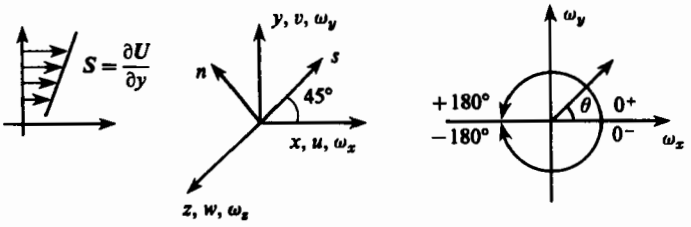

FIGURE 3. Coordinate system and sign convention for angle θ.

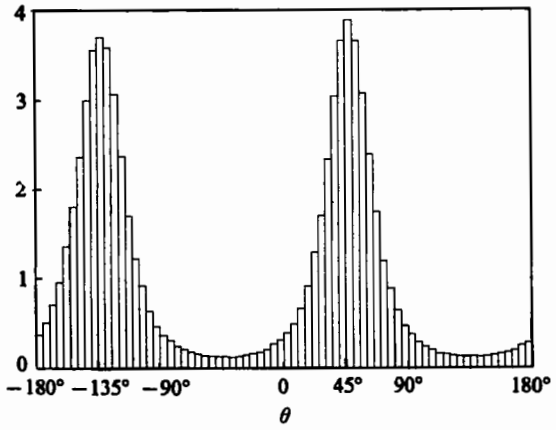

FIGURE 4. Distribution of the inclination angle of the projection of the vorticity vectors in (x, y)-planes; data weighted with the magnitude of the projected vorticity.

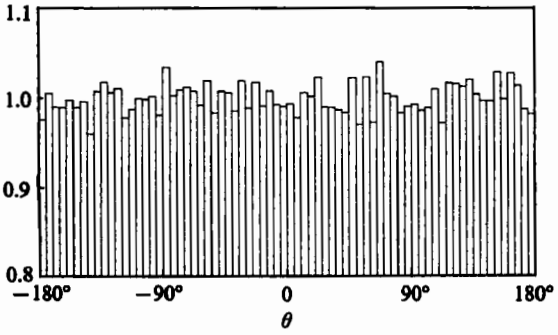

FIGURE 5. Distribution of the inclination angle of the projection of the vorticity vector in (x, y)-planes for the initial field; data weighted with the magnitude of the projected vorticity.

maximum stretching by the mean strain and its vorticity is increased. This result illustrates the importance of vortex stretching by *mean* shear to the dynamics of shear flows and indicates that planes inclined near 45° to the mean-flow direction are likely to contain strong vortical structures.

Figure 6 shows the two-point correlations of the three velocity components (at $St = 2.0$) with separation along the x-, s- and n-directions (see figure 3). The two-point correlation is defined as

$$R_{ab}(\boldsymbol{r}; t) = \frac{\overline{a(\boldsymbol{x}; t)\, b(\boldsymbol{x}+\boldsymbol{r}; t)}}{(\overline{a(\boldsymbol{x}; t)^2}\, \overline{b(\boldsymbol{x}; t)^2})^{\frac{1}{2}}},$$

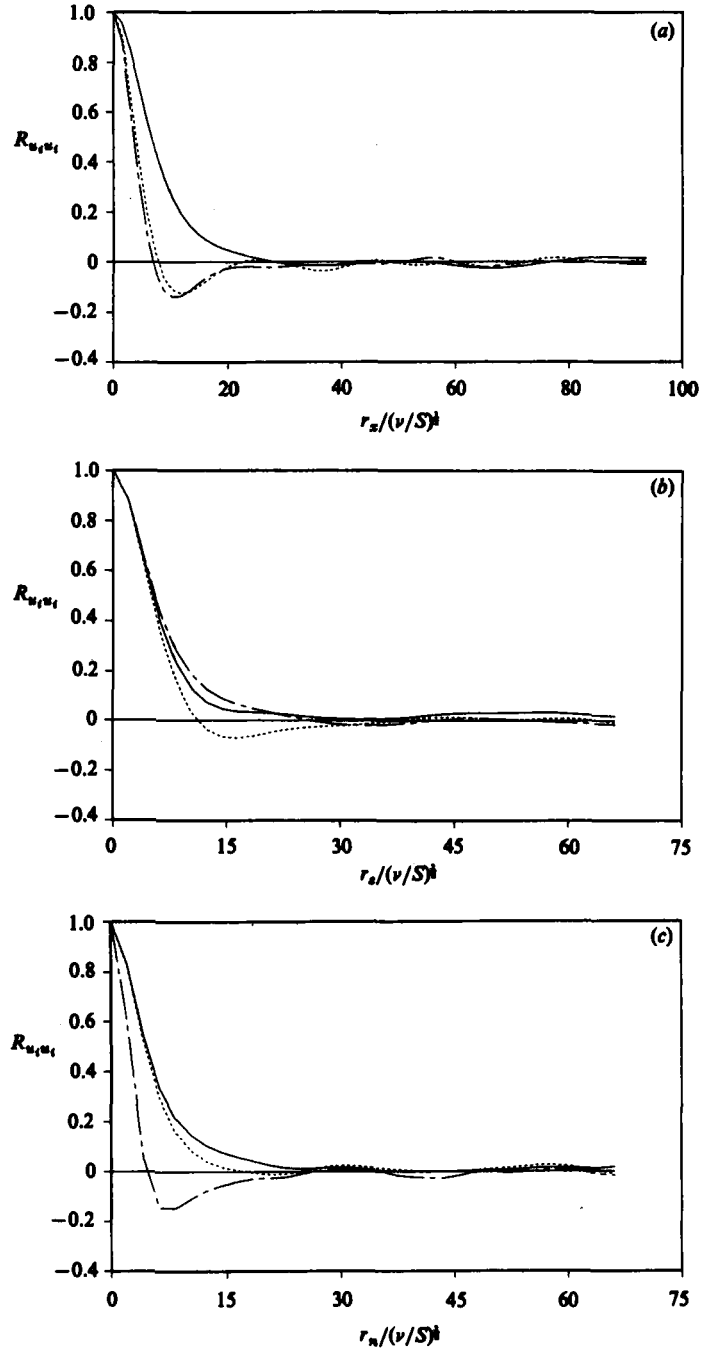

FIGURE 6. Two-point correlations of the velocity components with the direction of separation in the (*a*) x-direction; (*b*) s-direction; (*c*) n-direction. ——, R_{uu}; – – – –, R_{vv}; — — —, R_{ww}.

where $\boldsymbol{x}$ is the position of each point and $\boldsymbol{r}$ is the separation vector. The average in the above equation (and throughout this report) is taken over all three space dimensions; homogeneity implies that this is equivalent to an ensemble average over many flow fields. The separation distance has been non-dimensionalized by the lengthscale $(\nu/S)^{\frac{1}{2}}$. The most interesting feature of these correlations is the behaviour

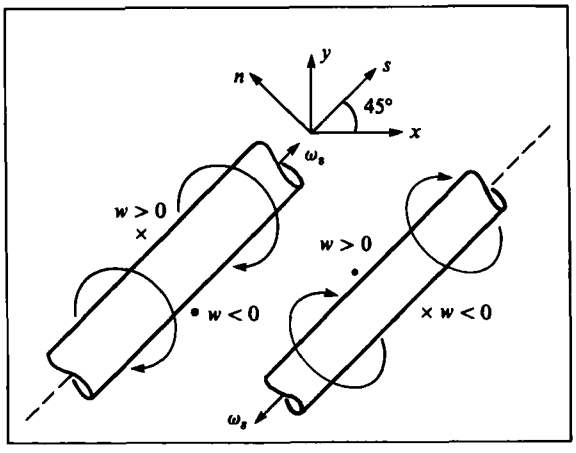

FIGURE 7. Sketch of the vortical structures inclined at 45° to the wall.

of R_{ww}, the correlation between the spanwise velocity fluctuations. In particular, $R_{ww}(r_s)$ does not become negative (i.e. it does not cross the abscissa to within statistical fluctuations), whereas the R_{ww} correlations with separations in other directions do cross the abscissa. This is consistent with a vortex tube inclined at 45° to the flow direction (see figure 7). Along the structure (s-direction) w-velocity maintains the same sign, whereas crossing through the vortex tube it changes sign.

Two-point correlations of vorticity, particularly those of $R_{\omega_s \omega_s}$, were examined to more precisely investigate the structure of the vorticity field (figure 8). Their behaviour strongly supports the presence of strong vortical tubes that are elongated and inclined at 45° to the mean-flow direction. The ω_s component of vorticity is well correlated over a considerably longer range along r_s than it is along separations in r_z and, especially, r_n (or r_x and r_y – not shown). Figure 8 also shows the substantial crossing apparent when $R_{\omega_s \omega_s}(r_z)$ is examined. This crossing indicates that a vortex tube of opposite sign is often located nearby in the z-direction. The very rapid decay of $R_{\omega_s \omega_s}(r_n)$ shown in figure 8(c) is expected because two-point correlations weight hairpins with high vorticity magnitudes heavily and such hairpins consist of highly stretched vortex filaments with small diameters. The slight negative region in figure 8(c) is probably a consequence of inadequate resolution of these strong but small-diameter vortices.

The instantaneous vorticity fields were analysed for direct evidence of the presence of hairpin vortices. Figure 9 shows the projection of vorticity vectors (at $St = 2.0$) on a randomly selected plane inclined at 45°. Hairpin vortices are clearly discernible, identified by two regions (legs) with opposite ω_s signs connected at the top (or bottom for inverted hairpins) by a region with $\omega_s = 0$ and finite ω_z. Note that this projection shows clearly only those hairpins with both legs in the (s, z)-plane. The projection of the vorticity vectors of the initial flow field ($St = 0$) on the same plane (figure 10) shows random vectors with no evident coherent structures.

A hairpin vortex can be displayed by vortex lines drawn in three-dimensional space. These lines are everywhere tangent to the vorticity vectors and are defined by

$$\frac{\mathrm{d}x}{\mathrm{d}s} = \frac{\omega}{|\omega|},$$

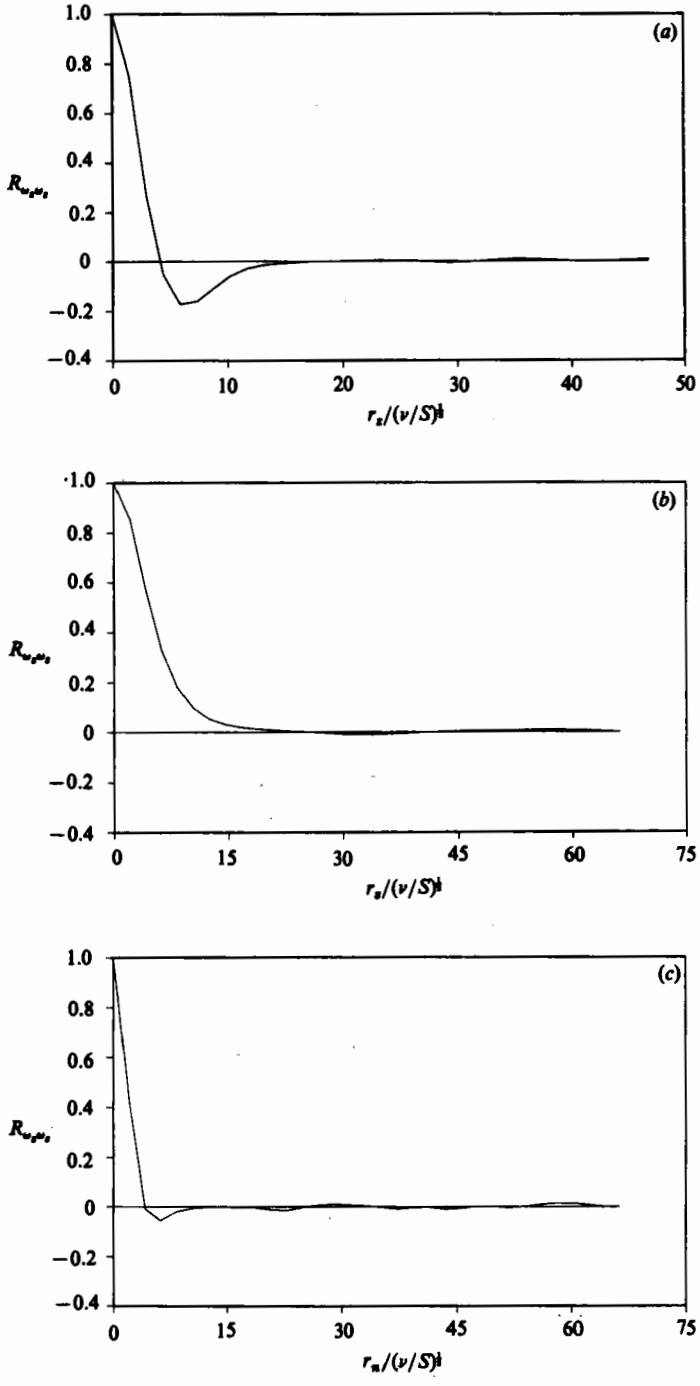

FIGURE 8. Two-point correlations of the ω_s vorticity with the direction of separation in the (*a*) z-direction; (*b*) s-direction; (*c*) n-direction.

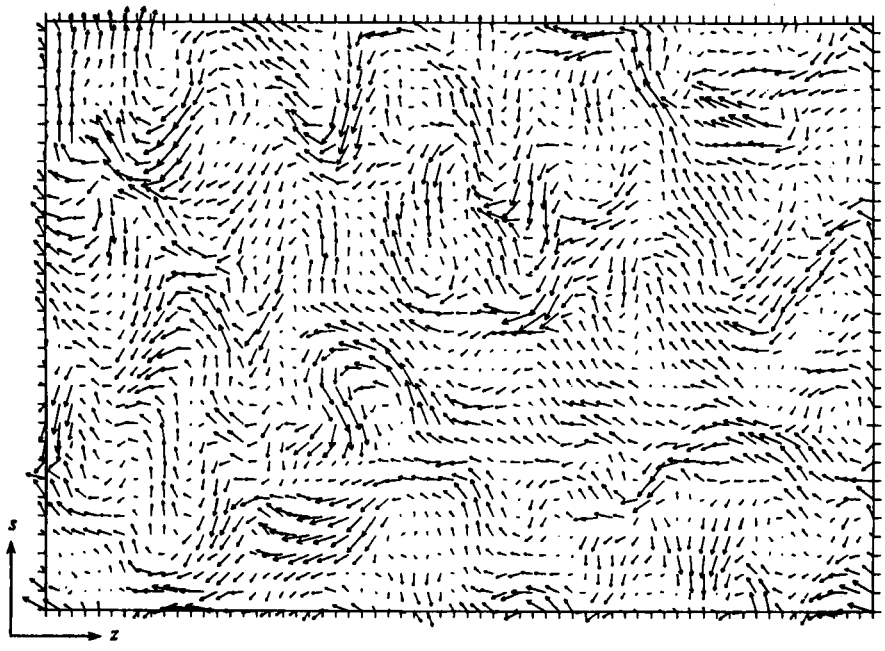

FIGURE 9. Projection of the instantaneous vorticity vectors on a plane inclined at 45°. Tick-marks represent the location of the computational grid.

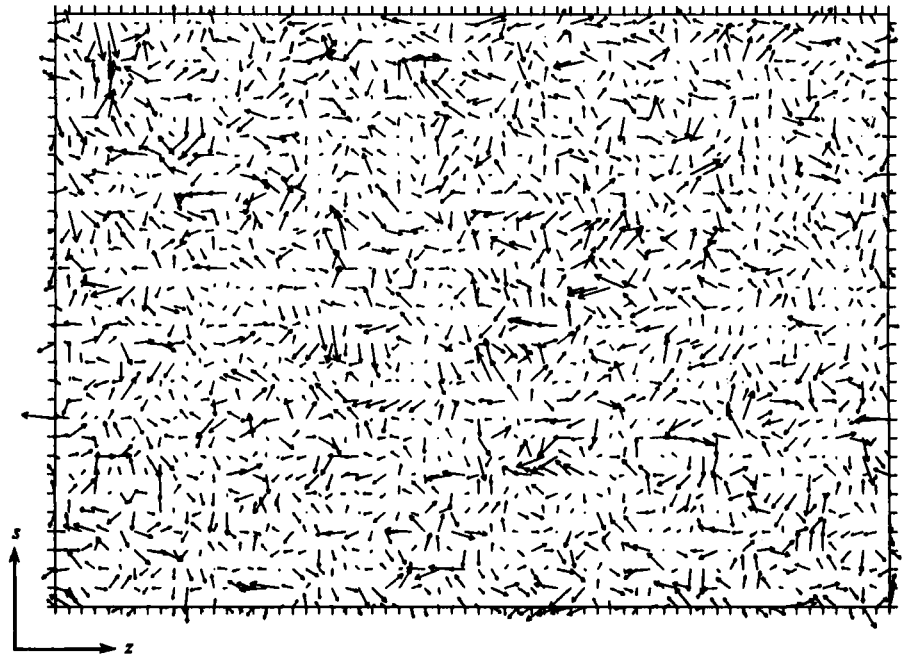

FIGURE 10. Projection of the initial-field vorticity vectors on the same plane as in figure 9. Tick-marks represent the location of the computational grid.

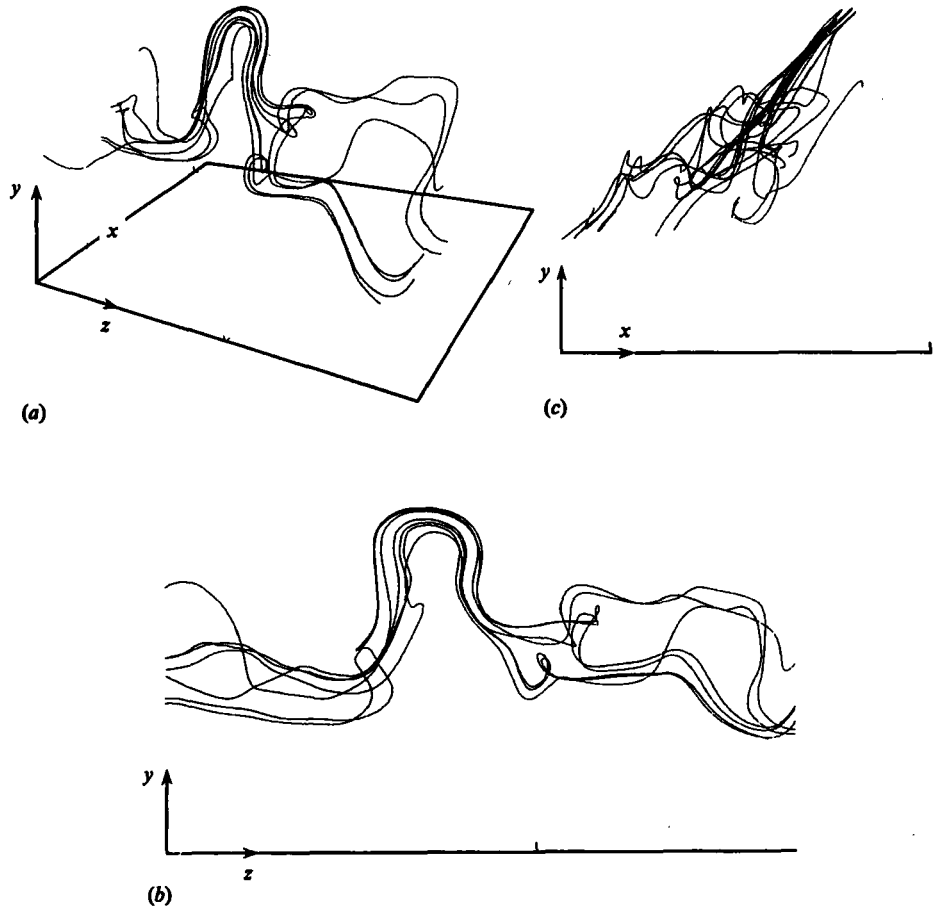

FIGURE 11. Typical vortex lines displaying a hairpin-like structure. (*a*) Three-dimensional view; (*b*) end-view (y, z)-plane; (*c*) side-view (x, y)-plane.

where s is the distance along the vortex line and $\boldsymbol{\omega}$ is the vorticity vector at point $\boldsymbol{x}$. Initial points of integration $\boldsymbol{x}_0$ were selected on the legs of the structures that appeared to be part of a hairpin in the vector plots. The vortex lines were then traced out by integrating the above equation. Figure 11 shows a typical collection of vortex lines which display a hairpin-like structure. The hairpin vortices are formed from the deformation or roll-up of sheets of transverse (mean) vorticity and generally do not have legs elongated in the x-or z-direction. In agreement with Hama's (1962) analysis, the tips of the hairpins have a Ω shape because of self-induction effects. However, this form of the tips is not as pronounced as that observed in channel flow. It can be shown that the uniform shear in this flow (in contrast to the reduced shear in the outer region of boundary layers) dominates the self-induction effects and inhibits the progressive deformation of the tip region into pronounced Ω shapes and ultimately into ring vortices (Moin, Leonard & Kim 1986). The hairpins traced out by this method generally have strong vorticity (about three times the r.m.s. vorticity, $\omega = (\overline{\omega_i \omega_i})^{\frac{1}{2}}$, and four to five times the mean vorticity S).

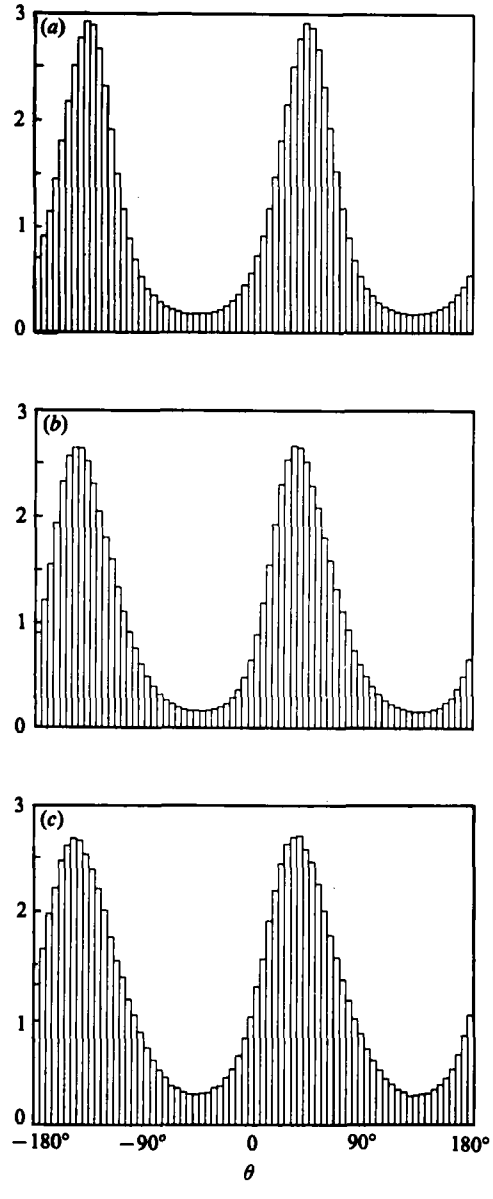

FIGURE 12. Distribution of the inclination angle of the projection of the vorticity vectors in (x, y)-planes at non-dimensional times $St = 4.0, 8.0, 14.0$; data weighted with the magnitude of the projected vorticity in the high-Reynolds-number simulation.

3.2. *High-Reynolds-number shear case*

Figure 12 shows the weighted distribution of the inclination angle of vorticity vectors θ at three dimensionless times ($St = 4.0$, 8.0 and 14.0). Again, the histograms show pronounced maxima near 45°. Starting at St of about 6, however, the histograms become noticeably skewed and their peaks move to lower angles, stabilizing between $\theta = 35°$–$40°$. The weighted histograms in figure 12 show this shift more dramatically than the corresponding unweighted plots, implying that it is the strong, highly

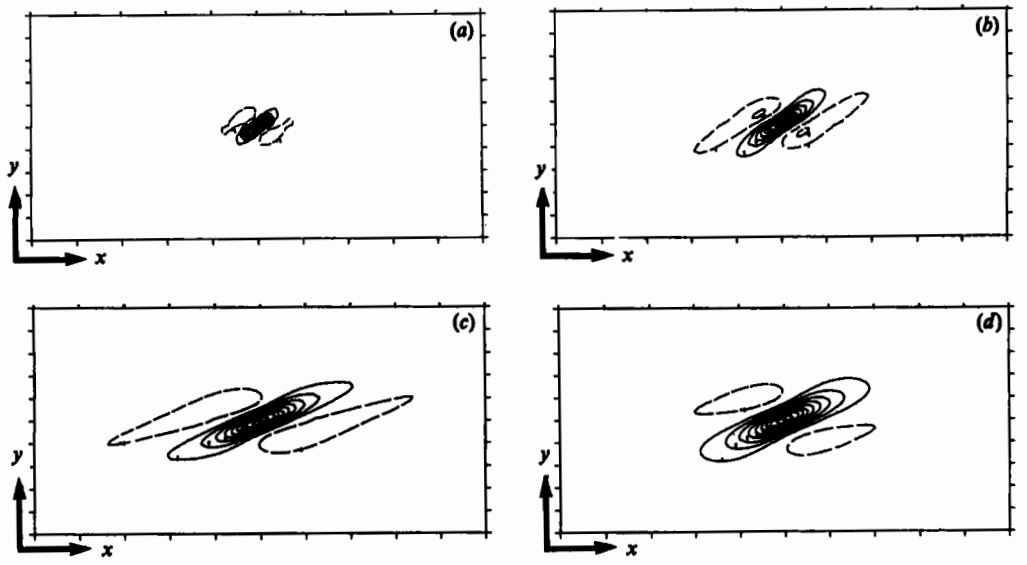

FIGURE 13. Two-point-correlation contour plots of $R_{ww}(r_x, r_y)$. (*a*) $St = 2.0$; (*b*) 4.0; (*c*) 8.0; (*d*) 14.0. Contour levels at multiples of 0.1 times the zero-separation value. Each side is one-quarter the computational box size in that direction.

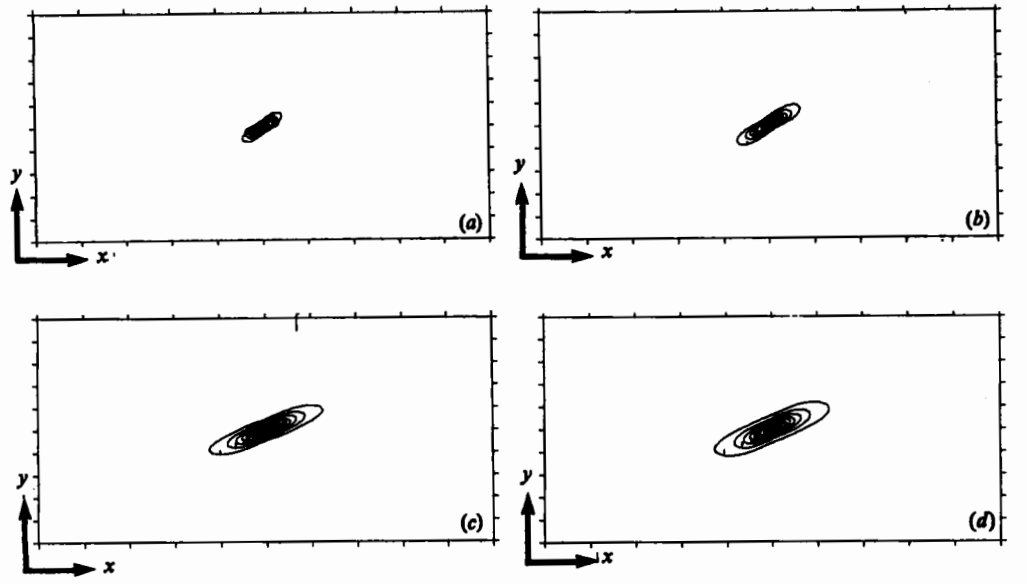

FIGURE 14. Two-point-correlation contour plots of $R_{\omega_z \omega_z}(r_x, r_y)$. (*a*) $St = 2.0$; (*b*) 4.0; (*c*) 8.0; (*d*) 14.0. Contour levels at multiples of 0.1 times the zero-separation value. Each side is one-quarter the computational box size in that direction.

stretched vorticity that lies at lower angles. The reason underlying this time development of the histograms becomes clearer if we look at the sequence of contour plots (figure 13) of the two-point correlation, $R_{ww}(r_x, r_y)$. Given an inclined vortical structure, the longest coherence in w-velocity is along the axis of the vortical tube. As St increases, the structure tends to be stretched and rotated. To ensure that the

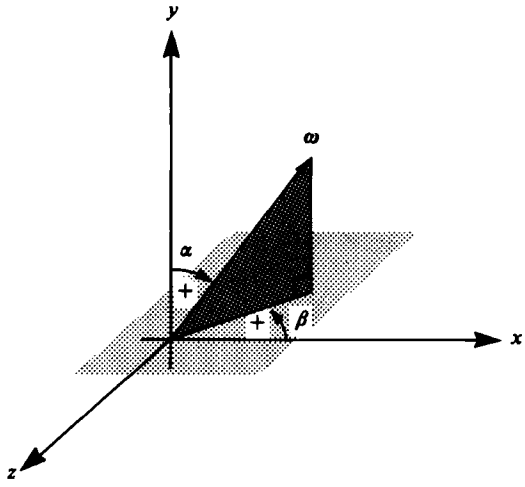

FIGURE 15. Sign convention for angles α and β.

R_{ww} velocity correlation was in fact indicative of vortical structure, contour maps of vorticity two-point correlations were also examined. Strictly speaking, we want to find which value of θ maximizes the correlation distance of $R_{\omega_\theta \omega_\theta}(r_x, r_y)$ where ω_θ is the component of vorticity in the θ-direction. This would require computing such correlations at all angles θ. However, given a strong, coherent vortical structure, we expect its components ω_1 and ω_2 to exhibit roughly the same behaviour as the vorticity along the axis of the structure. Given that our coherent structures typically lie in the range $\theta = 22°$–$45°$ the $R_{\omega_2 \omega_2}$ correlation behaviour would be expected to more closely approximate the $R_{\omega_\theta \omega_\theta}$ correlation along the structure than either $R_{\omega_1 \omega_1}$ or $R_{\omega_2 \omega_2}$. $R_{\omega_1 \omega_1}(r_x, r_y)$, $R_{\omega_2 \omega_2}(r_x, r_y)$, and $R_{\omega_3 \omega_3}(r_x, r_y)$ all showed the same qualitative behaviour, and $R_{\omega_3 \omega_3}(r_x, r_y)$ had almost exactly the same angle of maximum correlation as the $R_{ww}(r_x, r_y)$ correlation. Thus it appears that the w-velocity correlations are indeed good indicators of vortex structure in this flow. Figure 14 shows the time development of $R_{\omega_3 \omega_3}(r_x, r_y)$. Initially, the structure is stretched along $\theta = 45°$ by the mean strain, but as time goes on, the mean rotation tends to rotate the structures as they become highly stretched. By St of about 8, an equilibrium seems to have been reached between the mean rotation and some restoring force, possibly the self-induced motion due to the velocity field generated by the hairpin, and θ stabilizes near 22°. Note that although this is close in magnitude to the angle of the principal axes of the Reynolds stress tensor, it is of opposite sign and their similarity in magnitude appears coincidental.

At $St = 8.0$ the angle of the principal axes of the $\overline{\omega_i \omega_j}$ tensor is about 40°; it is slightly above this value at lower St values and slightly below at higher St. Although these values are in good agreement with the θ-histograms, they are substantially higher than the 22° obtained from the two-point correlations. As mentioned before, the two-point correlation function strongly favours the high-magnitude-vorticity structures. Figures 13 and 14 thus reflect the behaviour of the old, highly stretched vortex filaments and are not typical of most of the vorticity structure in these flows.

After the conclusion of this study, the two-point-correlation contour plots of $R_{ww}(y, y+r_y, r_x)$ were computed for the channel-flow database of Moin & Kim (1985). Here y is the inhomogeneous direction normal to the channel walls and x is the

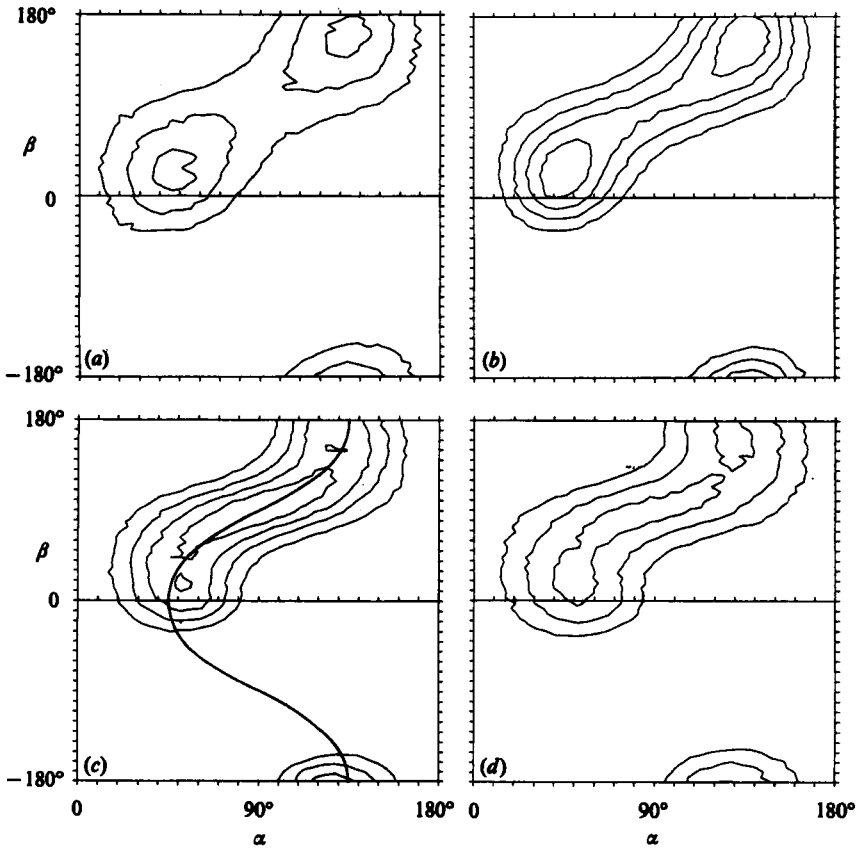

FIGURE 16. Two-angle probability-distribution function. (*a*) $St = 2.0$; (*b*) 4.0; (*c*) 8.0; (*d*) 14.0. The minimum contour level is 1000 and the levels are incremented by 500. 809 corresponds to the isotropic level.

streamwise direction. They show that in the regions away from the walls the direction of maximum correlation length is along θ of about 35°.

The two-angle probability-density function (p.d.f.) gives all the directional information of the vorticity vector and comparison of weighted and unweighted p.d.f.s indicates where the high-magnitude vorticity is located. The angle α is the angle between the vorticity vector and the y-axis; β is the angle between the projection of the vorticity vector in the (x, z)-plane and the x-axis. These angles and the sign convention used for the p.d.f.s are shown in figure 15. Figure 16 shows the time development of the unweighted two-angle p.d.f.s for the high-Reynolds-number simulation. Assuming that the primary structures contributing to the behaviour of the peak values in figure 16 are hairpin vortices, it can be seen that at early times the peak regions correspond to hairpin legs (i.e. $\alpha \approx 45°$, small β). As the flow develops, a central peak forms at the location corresponding to mean vorticity ($\alpha = 90°, \beta = 90°$). Also, as old hairpins are toppled by the mean rotation, the peaks corresponding to hairpin legs move toward $\alpha = 90°$. These two effects cause the p.d.f. to show a more S-like shape. It is interesting to note that lines of constant θ on these contour plots have an S-like shape roughly similar to the contour profiles. The bold

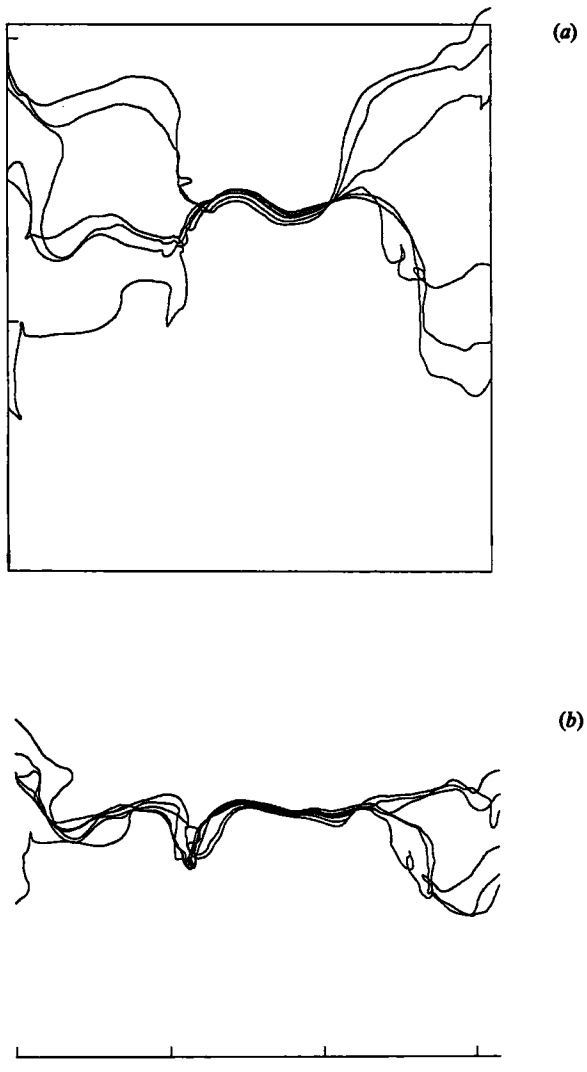

FIGURE 17. Vortex lines displaying a spanwise vortex structure. (*a*) top view; (*b*) rear view.

line in figure 16(*c*) represents the location of vectors lying in a plane inclined at $\theta = 45°$ in the p.d.f. plots. By about $St = 8.0$ an equilibrium is reached between the destruction of highly stretched, old hairpin vortices and the creation of newly developing structures. Beyond this point the two-angle probability distribution remains relatively unchanged.

The build-up of strong vorticity in the region corresponding to mean shear in the p.d.f. contour plots (figure 16) is clearly apparent by $St = 8.0$. Vorticity-vector plots and vortex lines in three-dimensional space (figure 17) confirm the existence of strong vortex filaments aligned with the mean vorticity. Since these structures do not develop until relatively late compared with the generation of hairpins, and since hairpins consist of much stronger vorticity than the mean, one might speculate that these vortex filaments are remnants of the tip region of old hairpin vortices. Since the tips of these vortices are aligned with the mean vorticity, they are not stretched

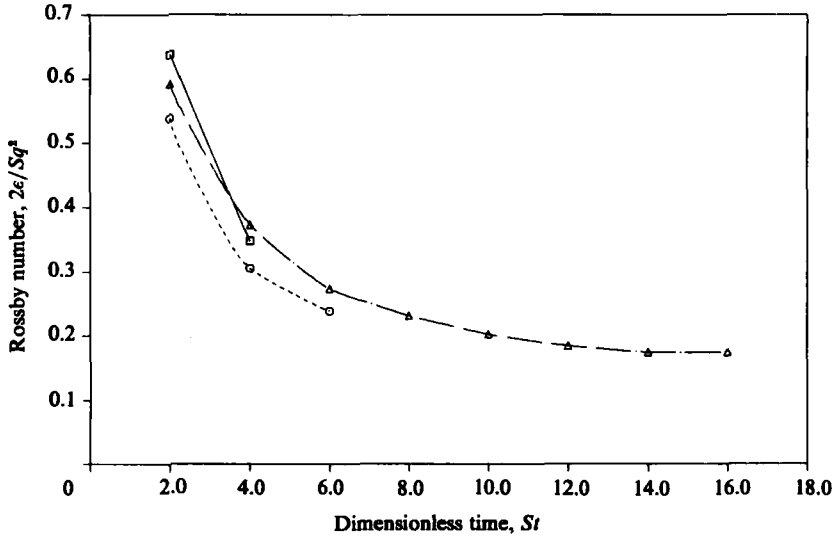

FIGURE 18. Rossby-number time development. □, low-Reynolds-number simulation; ○, intermediate-Reynolds-number simulation; △, high-Reynolds-number simulation.

by the mean strain, but only by induced motions of the fluctuating field. The legs of the hairpins, on the other hand, are stretched by the mean strain and so might be expected to be destroyed first. This would leave a high-magnitude vortex filament aligned with the mean that presumably would be more resistant to turbulent fluctuations than the comparatively weak mean vorticity.

A more plausible explanation for the formation of these strong spanwise filaments of vorticity is that they simply result from the imposed mean-rotation component of the mean shear. The mean deformation tensor for homogeneous turbulent shear flow can be decomposed into a plane-strain component and a mean-rotation component. The origin of hairpin vortices seems to be associated with the stretching of turbulent fluctuations along the direction of mean strain. It is therefore plausible to expect that another structure may result from the mean rotation. Hopfinger, Browand & Gagne (1982) have found that turbulence in a rotating tank tends to develop vortical tubes aligned with the mean vorticity. The strength of these vortices was determined to be up to 50 times that of the tank vorticity 2Ω, and of the same sign. Once formed, these structures were very persistent, having an average lifetime of about $St = 200$. The time required for the development of coherent vortices spanning the entire experimental-tank depth was found to be on the order of $St = 80$. It is thus reasonable that by $St = 8.0$ we have a number of strong vortices (about eight times the mean vorticity) coherent for roughly one-tenth the spanwise extent of our computational box.

For rotational flows at small Rossby number we expect Taylor–Proudman columns to develop because the mean rotation dominates the turbulence. For large Rossby numbers the effects of rotation will be negligible. In this flow, the characteristic velocity scale relative to the mean is q, the large-scale lengths can be represented by q^3/ϵ and the rotation rate is $\frac{1}{2}S$. This yields a Rossby number of $Ro = 2\epsilon/Sq^2$. The time development of Ro is shown in figure 18 for three simulations. For the developed shear fields the Rossby number is on the order of 0.2 and the behaviour is expected to be a combination of the two extremes decribed above. It should be noted that the

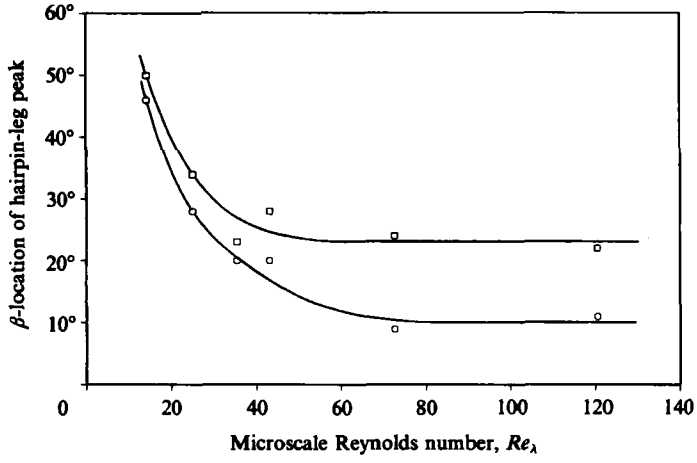

FIGURE 19. Dependence of β-location of hairpin legs on microscale Reynolds number. □, unweighted p.d.f. results; ○, weighted p.d.f. results.

strong spanwise vortex filaments do not form until the Rossby number drops to about 0.25 at $St = 6.0$. Hopfinger *et al.* (1982) found the critical Rossby number (below which strong vortical tubes formed) to be about 0.2 in their flow. For the low-Reynolds-number case we have $Ro = 0.637$ and the strong spanwise filaments were not observed in either the vector plots or the two-angle p.d.f.s.

The angle β_p corresponding to the peak contour associated with the hairpin legs is an indicator of the spanwise inclination of the legs. Using results from three different shear simulations, we see that this angle decreases with Re_λ as can be seen in figure 19. For the low-Reynolds-number case, β_p is about 50°; for the high-Reynolds-number case it is about 25° and appears to asymptotote to this value for Re_λ greater than about 70. Weighting the p.d.f.s by the magnitude of the vorticity vector always decreases β_p since the stronger hairpins have been stretched out more, causing their legs to become more nearly parallel to the x-direction. When weighted by the magnitude of the vorticity vector, β_p asymptotes to about 10° as Re_λ increases. This Reynolds-number dependence of β_p is consistent with the observed appearance of hairpin vortices in the vector plots. Figure 9 shows large, wavy structures with legs inclined in the spanwise direction. In contrast, we shall see in figure 20 that the hairpins of higher-Reynolds-number fields have their legs more nearly perpendicular to the z-direction.

Because hairpin legs typically lie at some non-zero β, projecting them into an (x, y)-plane results in a value of θ that is not simply the complement of α. From

$$\theta = \tan^{-1}\left(\frac{1}{\tan\alpha\cos\beta}\right)$$

we can determine how the variation of β manifests itself in the θ-histograms and in the two-point-correlation contour plots. For $\beta = 0°, \theta = 90° - \alpha$; for larger β, θ will correspond to a somewhat larger angle. For $\beta = 25°$ (high-Reynolds-number case), the difference between θ and $90° - \alpha$ is under 3° over a range of α near 45°. Taking $\beta = 50°$ (low-Reynolds-number case), however, yields a difference of 12°–13° for the same range of α. For the highly stretched hairpins (weighted p.d.f.) that have $\beta = 10°$, θ is less than 0.5° larger than $90° - \alpha$ for all α. It is thus clear that,

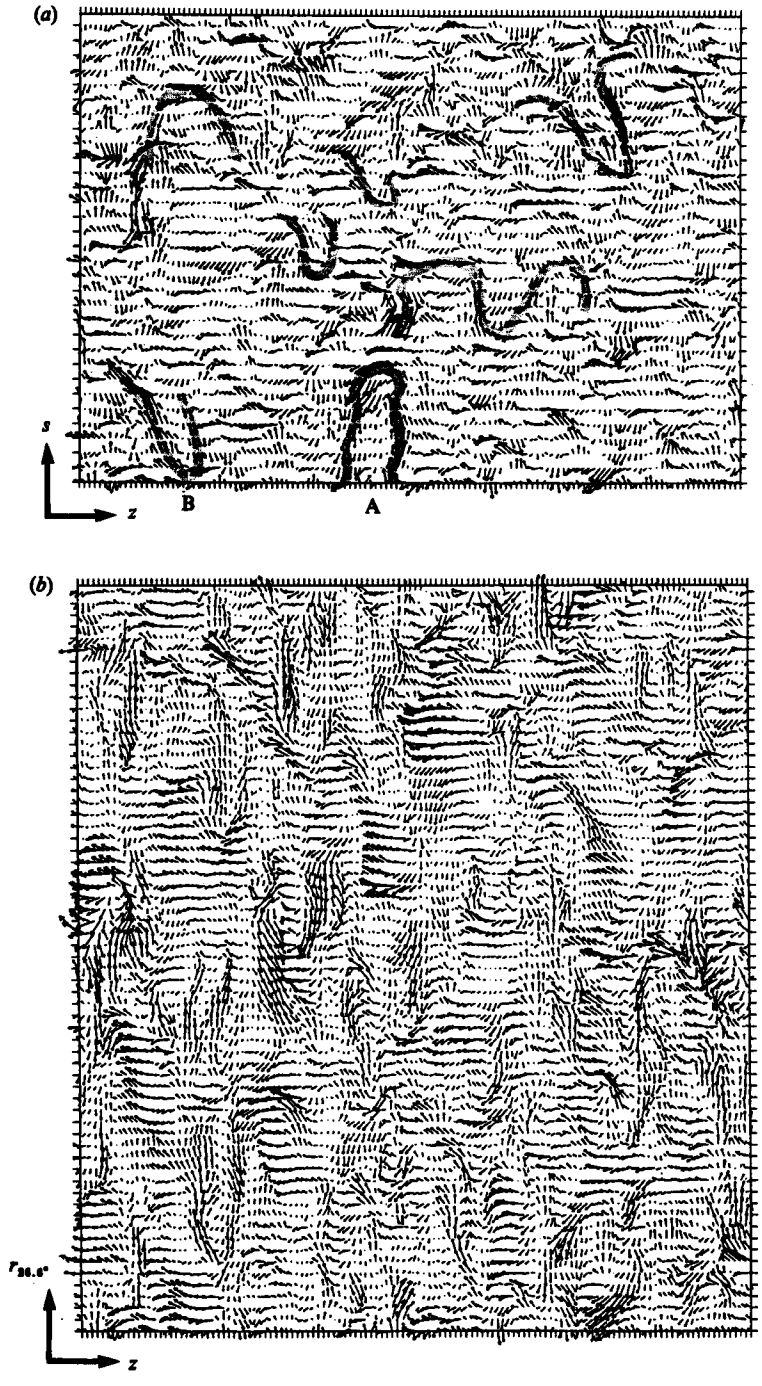

FIGURE 20. Projection of the instantaneous vorticity vectors on a plane inclined at (*a*) 45° and (*b*) 26.6° (from the high-Reynolds-number simulation at $St = 8.0$). In (*a*) some of the structures resembling hairpin vortices are shaded. Tick-marks represent the location of the computational grid.

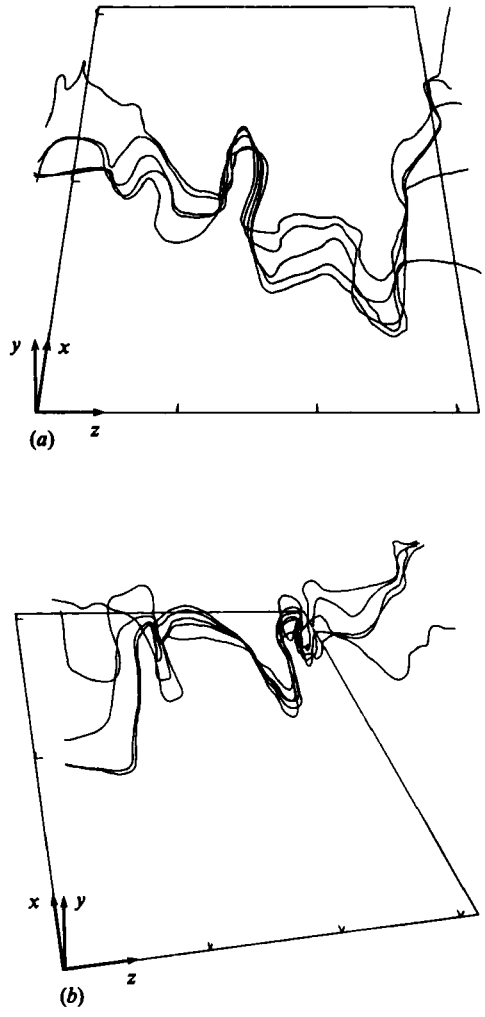

FIGURE 21. Vortex lines displaying hairpin-like structures. Vortex lines were initiated on the structures marked (*a*) A and (*b*) B in figure 20(*a*).

particularly for the low-Reynolds-number simulation, the α-location of the peak corresponding to hairpin legs in the two-angle p.d.f. is not simply the complement of the θ-location of the peak in the θ-histogram.

The projection of vorticity vectors at the dimensionless time $St = 8.0$ in a plane inclined at 45° to the flow direction is shown in figure 20(*a*). A number of hairpin vortices are discernible. However, they do not appear to be as pronounced nor quite as frequent as those in the low-Reynolds-number simulation. This is primarily due to the broadening of turbulence spectra with increasing Reynolds number. Since the two-point-correlation contour plots indicated that a number of large coherent structures could be found in planes inclined as low as 22°, we also examined the instantaneous-vorticity-vector projections onto a plane inclined at 26.6° (a computationally convenient value) to the flow direction. For larger St, where the two-point correlation indicated the presence of these low-angle structures, this resulted in some improvement in the detection of vortical structures (figure 20*b*). Drawing vortex

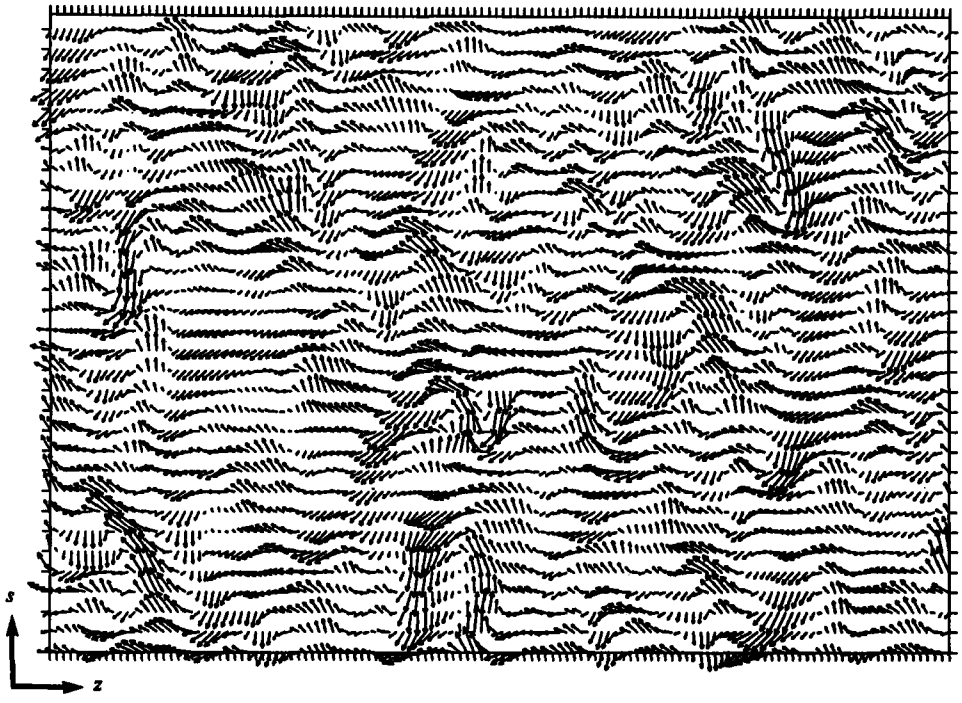

FIGURE 22. Projection of the filtered vorticity vectors on a plane inclined at 45°. From the high-Reynolds-number simulation at $St = 8.0$ (same view as figure 20*a*).

lines from points in the structures that appear to be hairpin vortices, we see that most of the hairpins have θ somewhere between these two extremes; the structures we observe are the projections of these hairpins in either of these two planes. In agreement with the two-point-correlation contour plots we see that the longest coherent structures are much more likely to be found in the plane inclined at 26.6° than 45°. Figure 21 shows vortex lines displaying two typical hairpin vortices traced starting from points in the two structures marked A and B in figure 20(*a*). In this homogeneous flow, 'inverted' hairpins are equally as likely as 'upright' hairpins. One of each is shown. Hairpins traced out in this fashion have vorticity that is roughly three times the r.m.s. vorticity and eight to nine times the mean vorticity.

By examining many simulations of homogeneous turbulent shear flow it has been found that hairpin vortices cannot form if the fluctuating vorticity field is dominated by the mean shear. This is not surprising since the formation of a hairpin requires turbulent vorticity fluctuations that are strong enough to overcome the mean vorticity and direct the total vorticity vector roughly in the ω_s direction. Hairpin vortices are common in fields where the r.m.s. fluctuating vorticity is greater than about 1.5 times the mean. In homogeneous flows, the ratio of the r.m.s. vorticity to the mean vorticity ω'/S scales like the microscale turbulence Reynolds number over Sq^2/ϵ. The simulations and experiments show Sq^2/ϵ reaching an asymptotic value of about 12 in this flow, indicating that ω'/S increases with Reynolds number. The low-Reynolds-number case has $\omega'/S = 1.63$. For the high-Reynolds-number simulation ω'/S increases from 2.29 at $St = 8.0$ to 3.43 at $St = 16.0$. In the experimental work, done at substantially higher Reynolds numbers, ω'/S ranges from about 7.7 to roughly 10.2.

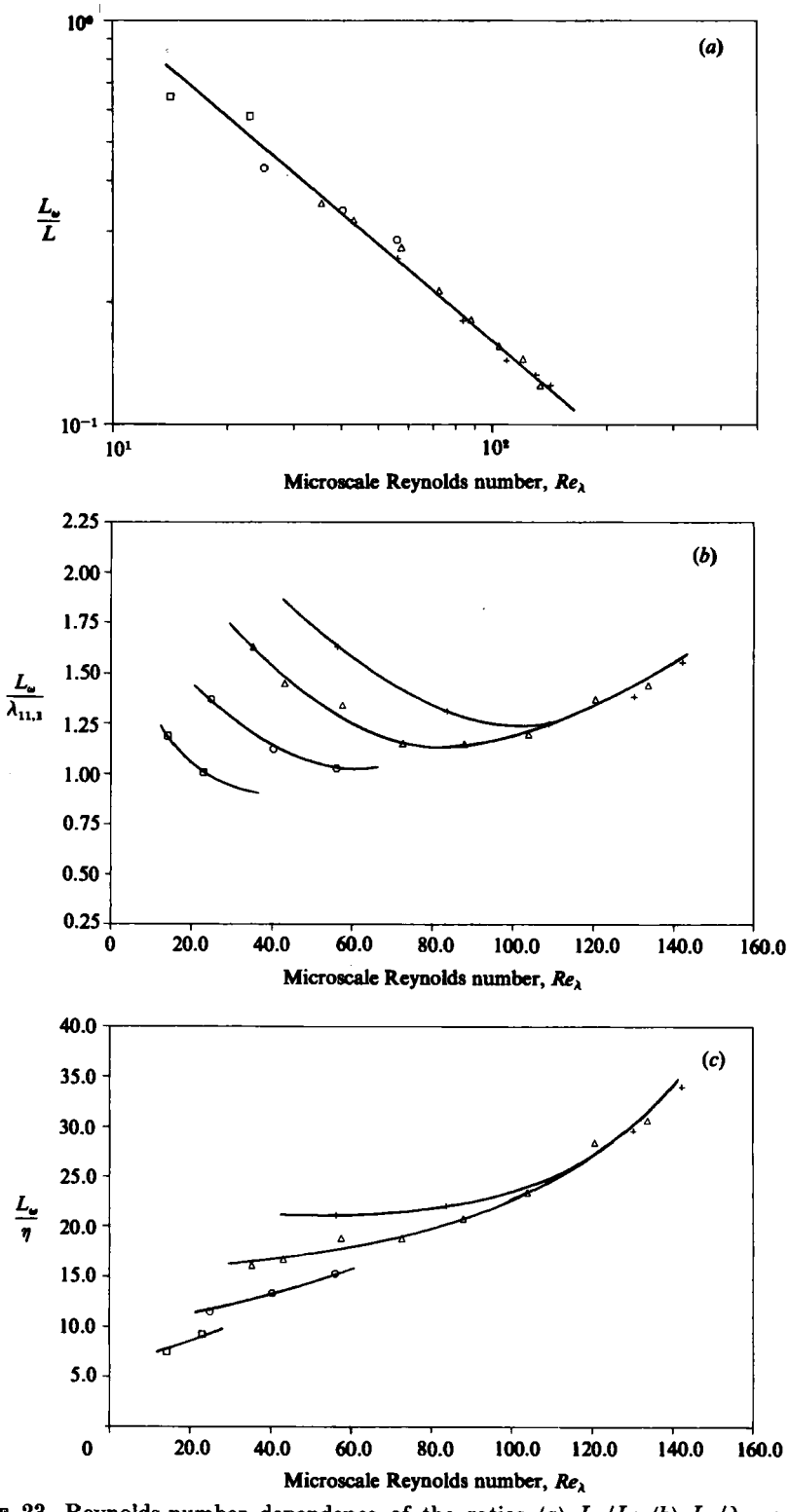

FIGURE 23. Reynolds-number dependence of the ratios (a) L_ω/L; (b) $L_\omega/\lambda_{11,1}$; (c) L_ω/η. □, low-Reynolds-number simulation; ○, intermediate-Reynolds-number simulation; △, +, high-Reynolds-number simulations.

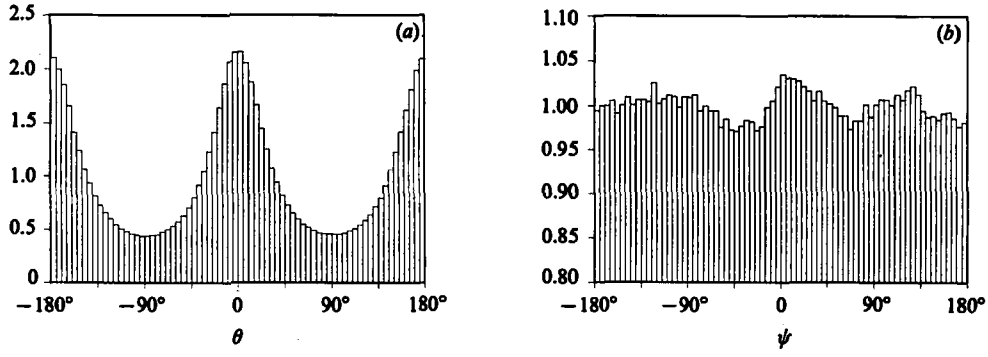

FIGURE 24. Distribution of the inclination angles of the projection of the vorticity vectors for axisymmetric contraction in (*a*) (x, y)-planes and (*b*) (y, z)-planes.

In order to determine whether the hairpins were actually disappearing, or were simply being obscured by small-scale vorticity, we filtered these fields with a Gaussian filter. The removal of high-wavenumber background vorticity allows the characteristic hairpin vortices to be viewed more clearly, as seen in figure 22 (compare with figure 20*a*). Note that the hairpin structures in figure 22 are clearly evident, even without the shading used in figure 20(*a*). The fact that a filtered high-Reynolds-number field is qualitatively similar to a low-Reynolds-number field is indicative of the fact that hairpin vortices are present in higher-Reynolds-number fields where small-scale vorticity may obscure them. Filtering the flow yields a field that has complete capture of the dissipation scales. Because the same hairpins are still evident in this field we can be assured that the original field adequately captured the relevant scales for the study of these large-scale vortical structures.

To further address the question of whether one can extrapolate the present results to high-Reynolds-number flows (i.e. whether the hairpins continue to persist at very high Reynolds numbers), the size of the hairpins was examined as a function of Re_λ. The distance to the negative peak of the $R_{\omega_3\omega_3}(r_z)$ two-point-correlation profile is an indicator of the average hairpin size L_ω, this being representative of the distance between the centres of the hairpin legs. Taking $L = q^3/\epsilon$ as the characteristic large-eddy lengthscale and the Kolmogorov scale $\eta = (\nu^3/\epsilon)^{\frac{1}{4}}$ as a measure of small-scale length, the Reynolds-number dependence of L_ω/L, $L_\omega/\lambda_{11,1}$ and L_ω/η was examined using data from four shear runs at several non-dimensional times St. The ratio L_ω/L collapses the data from all runs onto one characteristic curve that indicates a power-law dependence on Re_λ, as seen in figure 23(*a*). Whether L_ω/L eventually does drop to zero or asymptotes to a positive constant is impossible to determine without computations with an order of magnitude more grid points. We can, however, be reasonably sure that hairpins persist to at least Re_λ of about 200–300, which is on the order of the experimental Reynolds numbers reported in table 1. $L_\omega/\lambda_{11,1}$ increases with Reynolds numbers for developed shear flows (figure 23*b*), implying that hairpin vortices grow faster than the longitudinal microscale. This provides strong evidence that hairpins are not limited to low-Reynolds-number flows. It should also be noted that because L_ω/η continually increases with Re_λ (figure 23*c*), the hairpins are not associated with the smallest scales in the flow.

A brief examination of the velocity fields was also conducted. For both Reynolds numbers contour plots of instantaneous uv showed very intermittent regions of production, similar to the behaviour observed in turbulent channel flow (Moin 1985).

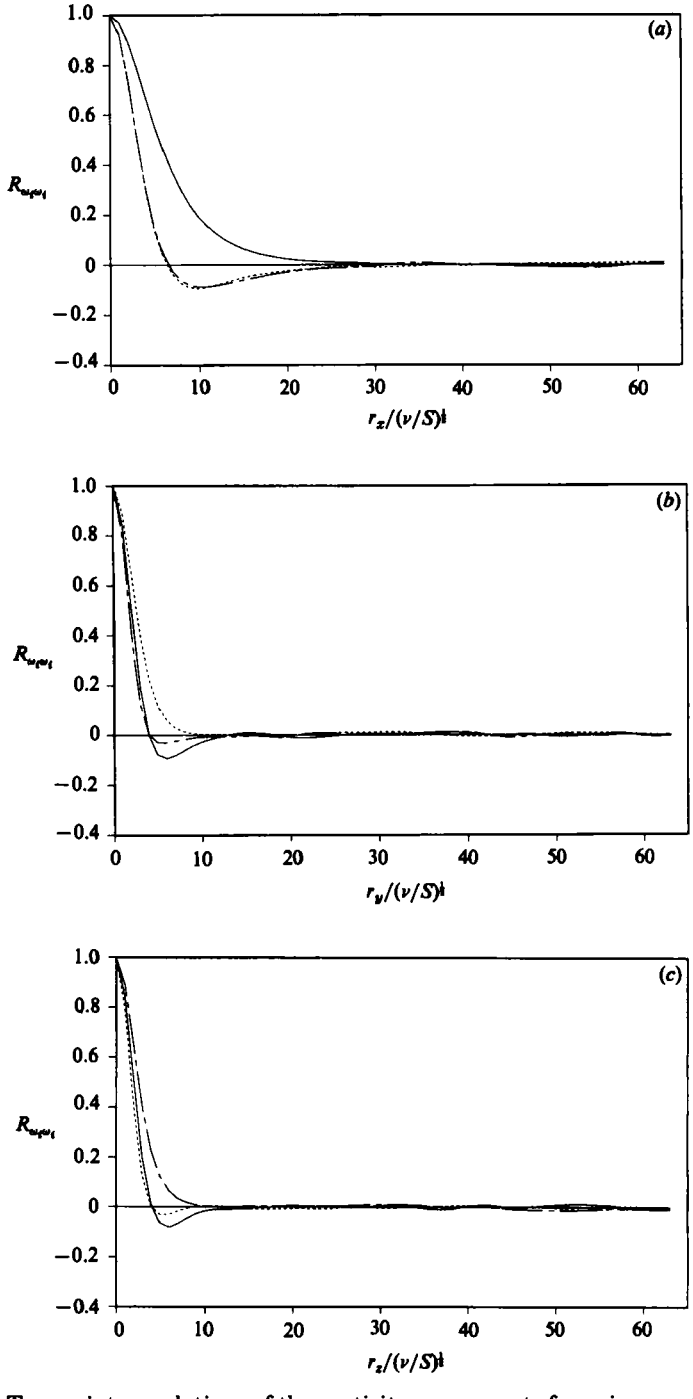

FIGURE 25. Two-point correlations of the vorticity components for axisymmetric contraction with the direction of separation in the (*a*) x-direction; (*b*) y-direction; (*c*) z-direction. ——, $R_{\omega_1\omega_1}$; – – – –, $R_{\omega_2\omega_2}$; — — —, $R_{\omega_3\omega_3}$.

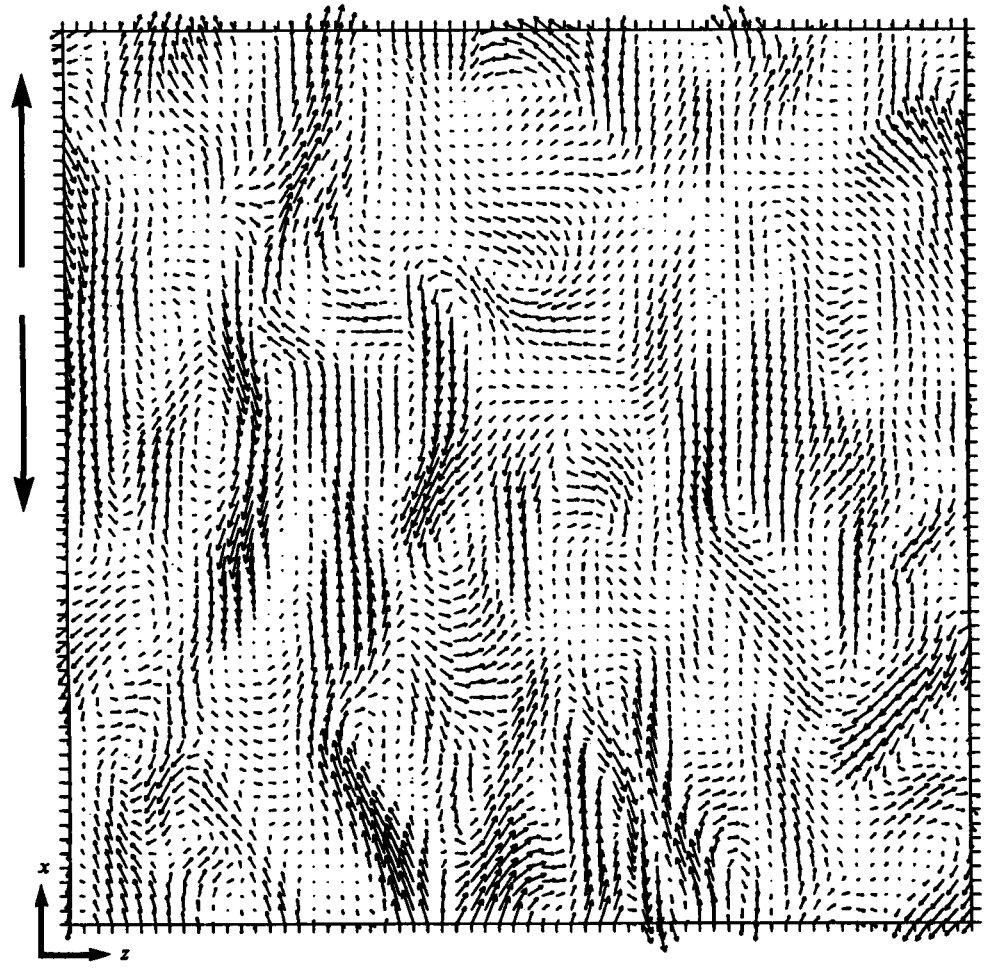

FIGURE 26. Projection of the instantaneous vorticity vectors for axisymmetric contraction on an (x, z)-plane. Tick-marks represent the location of the computational grid.

In contrast to the channel-flow results, no streaks were observed in contour plots of u, but the contours were slightly elongated in the x-direction. In the near-wall region where streaks were observed in the channel-flow simulation $SL_{11,1}/q$ was on the order of 100 ($L_{11,1}$ being the integral lengthscale of the $R_{uu}(r_x)$ correlation); the corresponding values for our homogeneous shear cases (see table 1) are substantially lower, about 2.6.

4. Structure of the vorticity fields in the irrotational-straining-flow simulations

4.1. *Axisymmetric contraction*

For the irrotational straining fields we examine not only the inclination angle θ, but also

$$\psi = \tan^{-1}(\omega_y/\omega_z).$$

In the homogeneous shear cases, ψ was dominated by the mean shear and was less informative. The histograms for the axial-contraction case are shown in figure 24 (all

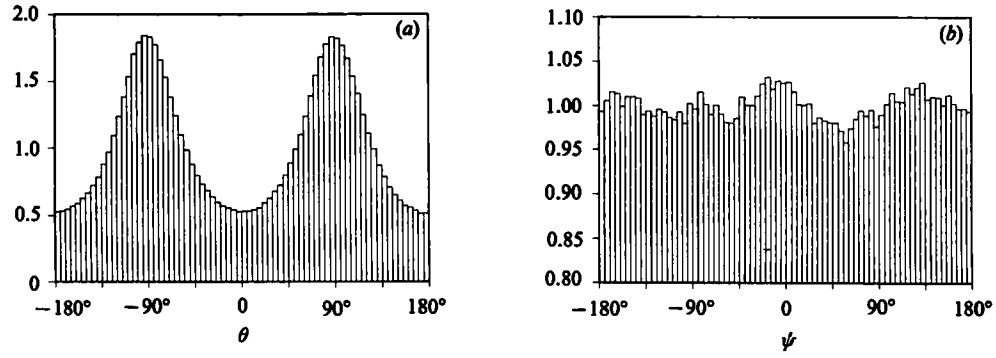

FIGURE 27. Distribution of the inclination angles of the projection of the vorticity vectors for axisymmetric expansion in (*a*) (x, y)-planes and (*b*) (y, z)-planes.

results for this case are for a total strain of 3.32). It is immediately apparent that the vorticity is being pulled in the direction of positive strain and is isotropic in ψ. Weighting the θ-histogram by the magnitude of the vorticity vector results in a higher maximum-to-minimum ratio of 12:1 (compared with just under 5:1 for the unweighted histogram), indicating, as in the shear-flow cases, that it is the large-magnitude, highly stretched vorticity that is more likely to be found aligned with the expansive mean strain. The histograms are symmetric around their peaks.

Figure 25 shows the two-point correlations of the components of the vorticity vector. They suggest the presence of longitudinal vortices elongated in x, the direction of expansive strain. The similarity between figure 25(*b* and *c*) is due to the axisymmetric nature of the flow. The velocity correlations are also well correlated to substantially greater separations in the x-direction than in the other directions.

The instantaneous vorticity vectors are shown in figure 26. The bold arrows indicate the direction of mean strain. Coherent vortex filaments elongated in the straining direction are visible. Three-dimensional vortex lines are not as informative for irrotational straining flows as for the shear flow because in the absence of mean shear a vortex line will wander around the computational box a number of times, passing through many different structures before finally intersecting a boundary.

4.2. *Axisymmetric expansion*

The unweighted histograms at a total strain of 3.32 are shown in figure 27. The θ-histogram has symmetric peaks at $\pm 90°$, indicating, as expected, that the vorticity is compressed into (y, z)-planes. Weighting by the magnitude of the vorticity vector increases the maximum-to-minimum ratio from about 3.5:1 to about 5.5:1. This increase is less than that observed in the other flows because the expansive strain is spread over two dimensions instead of being concentrated in one direction. The ψ-histogram is isotropic owing to the flow axisymmetry. This leads one to expect vortical structures randomly located in (y, z)-planes. Two-point correlations of vorticity (figure 28) show little correlation in the x-direction. The y- and z-correlations are similar to each other, as expected by axisymmetry.

Figure 29 shows a typical instantaneous vorticity-vector plot in a (y, z)-plane. It is difficult to see a characteristic structure in this flow. The (y, z)-plane has no preferred direction (figure 27) and although there are many ring-like structures, there are also regions of strong, coherent vorticity that are not part of a ring.

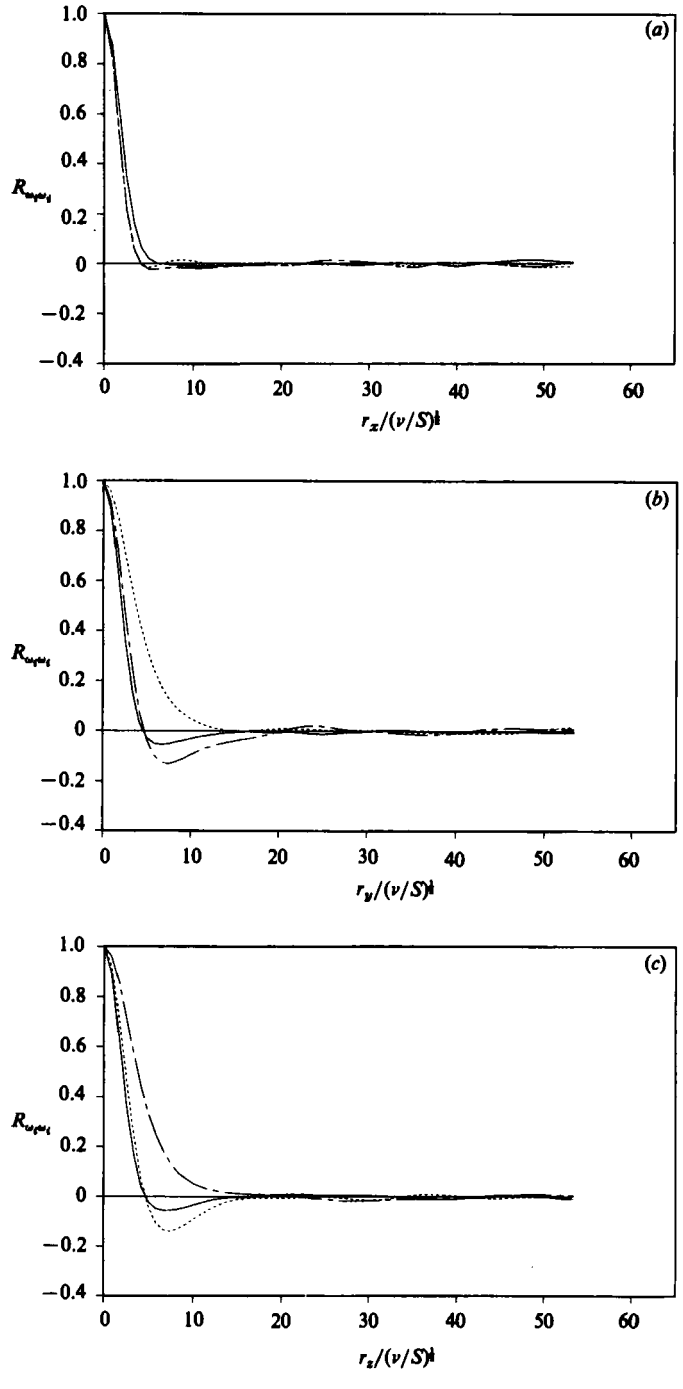

FIGURE 28. Two-point correlations of the vorticity components for axisymmetric expansion with the direction of separation in the (*a*) x-direction; (*b*) y-direction; (*c*) z-direction. ——, $R_{\omega_1\omega_1}$; – – – –, $R_{\omega_2\omega_2}$; — — —, $R_{\omega_3\omega_3}$.

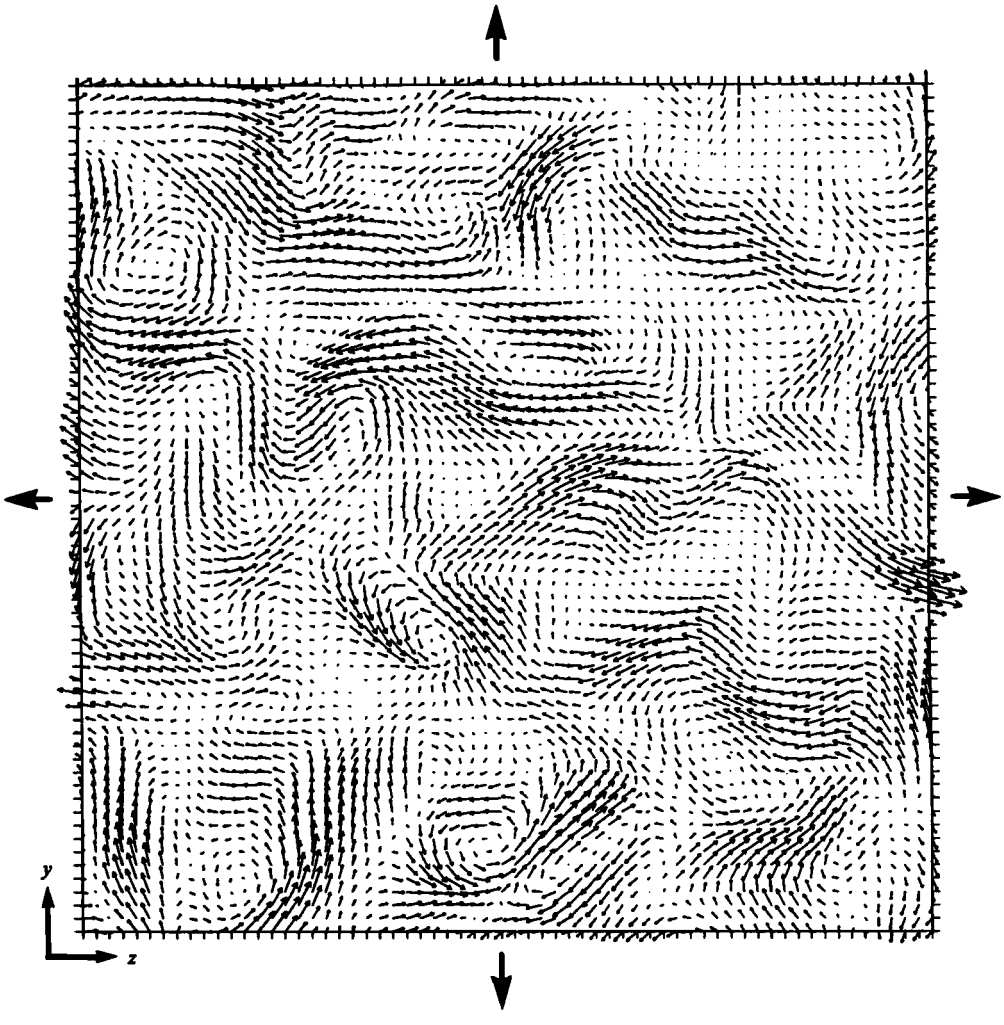

FIGURE 29. Projection of the instantaneous vorticity vectors for axisymmetric expansion on an (y, z)-plane. Tick-marks represent the location of the computational grid.

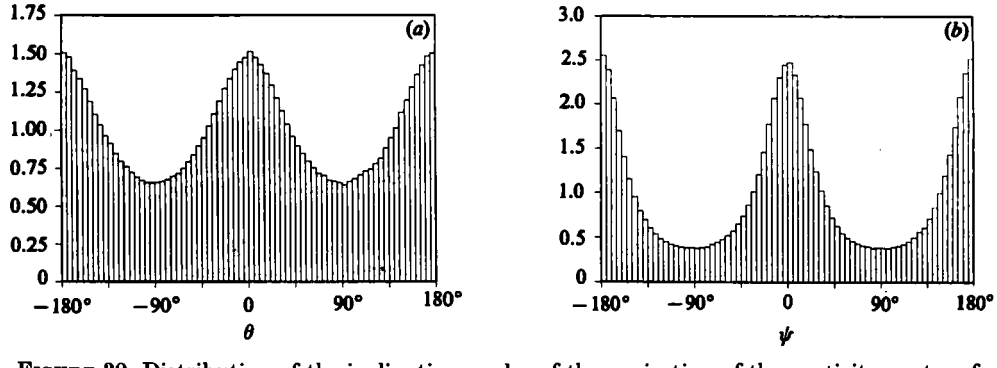

FIGURE 30. Distribution of the inclination angles of the projection of the vorticity vectors for plane strain in (*a*) (x, y)-planes and (*b*) (y, z)-planes.

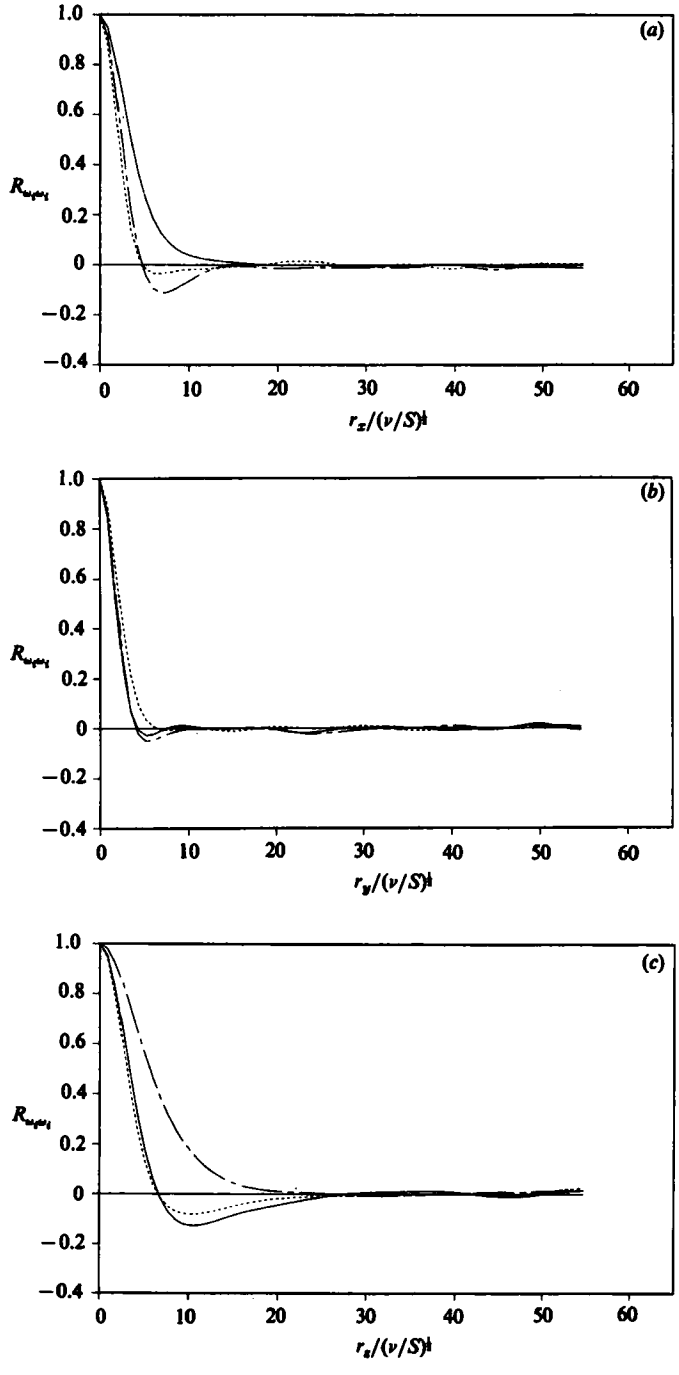

FIGURE 31. Two-point correlations of the vorticity components for plane strain with the direction of separation in the (*a*) x-direction; (*b*) y-direction; (*c*) z-direction. ——, $R_{\omega_1\omega_1}$; – – – –, $R_{\omega_2\omega_2}$; — — —, $R_{\omega_3\omega_3}$.

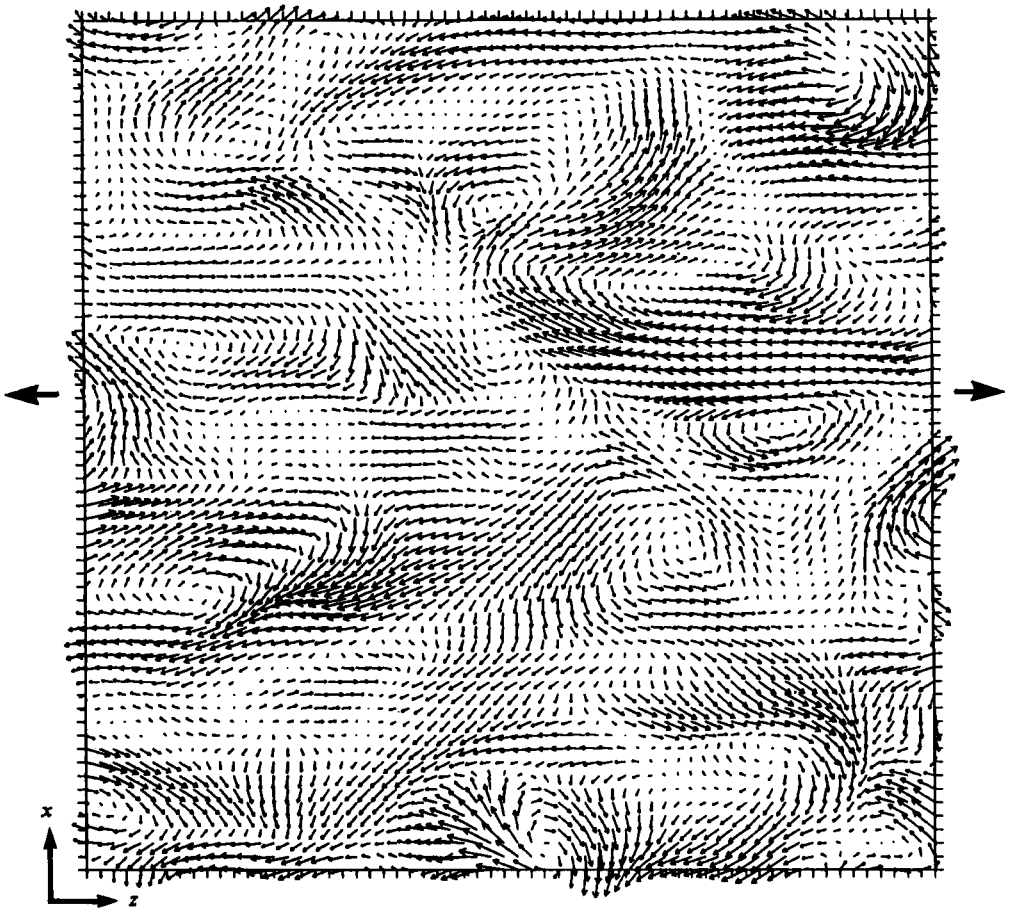

FIGURE 32. Projection of the instantaneous vorticity vectors for plane strain on an (x, z)-plane. Tick-marks represent the location of the computational grid.

4.3. *Plane strain*

At a total strain of 4.00, we see that both the θ-and ψ-histograms (figure 30) peak symmetrically at around 0° and 180°. Weighting the histograms changes the θ-distribution negligibly but increases the maximum-to-minimum ratio of the ψ-distribution from 6:1 to 17:1. The stretching in this flow is occurring in the z-direction, and thus it is expected that the high-magnitude, stretched vorticity is at $\psi = 0°$ and 180°. The increased magnitude of these stretched filaments is manifested in the increased maximum-to-minimum ratio of the weighted ψ-histogram. The compression in the y-direction does cause θ to peak at 0° and 180°, but does not strongly affect the magnitude of the vorticity because the weighted θ-histogram is almost identical with its unweighted counterpart. It appears that compressing a vortex filament does not tend to fatten it, but rather causes it to change direction or buckle, weakening it little if at all.

The two-point correlations shown in figure 31 show coherent vortical structures elongated in the direction of stretching, z, and short in the direction of compression, y. We also observe some elongation in x probably caused by the buckling of vortex filaments. The instantaneous vorticity vectors plotted in a typical (x, z)-plane are

shown in figure 32. We see elongated structures similar to axisymmetric contraction vortices and a few ring-like structures similar to those observed in the axisymmetric expansion flow. The strain-rate tensor in the plane-strain flow can be written as a linear combination of the strain-rate tensors for axisymmetric-contraction and axisymmetric-expansion flows. This leads to some speculation as to whether vortex structure is qualitatively also additive.

5. Conclusions

The structure of the vorticity field in homogeneous turbulent shear flow and in homogeneous irrotational straining flows has been examined using a database generated by direct numerical solution of the unsteady Navier–Stokes equations. In all cases strong evidence for the presence of coherent vortical structures was found. The initially isotropic vorticity fields were rapidly affected by imposed mean strain and the rotation component of mean shear and developed accordingly. The pulling of vortex filaments by the mean flow causes them to align with the direction of expansive strain and be stretched. This results in high-magnitude vorticity being especially aligned in the direction of expansive strain. Compression of vortex filaments tends to cause them to change direction or buckle, weakening them little if at all. Compressing a vortex filament is thus not simply the inverse of stretching. In the homogeneous-shear-flow cases, the roll-up of mean vorticity into characteristic hairpin vortices was clearly observed. The average spacing between the hairpin legs L_ω was found to increase faster than the Taylor microscale as Reynolds number increased, indicating that hairpin vortices are not simply a low-Reynolds-number phenomenon. The results of the present study and of a similar study in turbulent channel flow support the assertion that hairpin vortices are an important vortical structure in all turbulent shear flows. The similarity in vortex structure between the homogeneous shear flow and inhomogeneous channel flow gives strong justification for the study of homogeneous 'building-block' flows as a stepping stone to understanding more complex flows. The absence of mean shear in the homogeneous irrotational straining flows precludes the presence of hairpin-like vortices. Viewing two-dimensional instantaneous vector plots in the plane of mean strain does show coherent vortex structure, however. Axisymmetric-contraction flows develop elongated vortical structures in the stretching direction, and axisymmetric-expansion flows show no unique structure but have a number of ring-like structures present. Plane-strain flows appear to contain some combination of the structures observed in the axisymmetric cases.

We are indebted to Dr Robert S. Rogallo, Professor William C. Reynolds, and Dr Moon J. Lee for helpful discussions during the course of this work. The results presented in figures 22 and 23 sprang from discussions with Professor Peter Bradshaw of Imperial College for which we are very grateful.

REFERENCES

BURGERS, J. M. 1948 A mathematical model illustrating the theory of turbulence. In *Advances in Applied Mechanics*, Vol. 1 (ed R. von Mises & T. von Kármán), p. 171. Academic Press.

CHAMPAGNE, F. H., HARRIS, V. G. & CORRSIN, S. 1970 Experiments on nearly homogeneous shear flow. *J. Fluid Mech.* **41**, 81.

HAMA, F. R. 1962 Progressive deformation of a curved vortex filament by its own induction. *Phys. Fluids* **5**, 1156.

HEAD, M. R. & BANDYOPADHYAY, P. 1981 New aspects of turbulent boundary layer structure. *J. Fluid Mech.* **107**, 297.

HARRIS, V. G., GRAHAM, A. H. & CORRSIN, S. 1977 Further experiments in nearly homogeneous turbulent shear flow. *J. Fluid Mech.* **81**, 657.

HOPFINGER, E. J., BROWAND, F. K. & GAGNE, Y. 1962 Turbulence and waves in a rotating tank. *J. Fluid Mech.* **125**, 505.

KIM, J. & MOIN, P. 1986 The structure of the vorticity field in turbulent channel flow. Part 2. Study of ensemble-averaged fields. *J. Fluid Mech.* **162**, 339.

LEE, M. J. & REYNOLDS, W. C. 1985 On the structure of homogeneous turbulence. In *Proc. of the Fifth Symp. Turbulent Shear Flows, Cornell University, Ithaca, New York, August 7–9, 1985.*

MOIN, P. 1985 High Reynolds shear stress motions in the wall region. *Bull. Am. Phys. Soc.* **30**, 1723.

MOIN, P. & KIM, J. 1985 The structure of the vorticity field in turbulent channel flow. Part 1. Analysis of the vorticity fields and statistical correlations. *J. Fluid Mech.* **155**, 441.

MOIN, P., LEONARD, A. & KIM, J. 1986 Evolution of a curved vortex filament into a vortex ring. *Phys. Fluids* **29**, 955.

ROGALLO, R. S. 1981 Numerical experiments in homogeneous turbulence. *NASA TM* 81315.

TAVOULARIS, S. & CORRSIN, S. 1981 Experiments in nearly homogeneous turbulent shear flow with a uniform mean temperature gradient. Part 1. *J. Fluid Mech.* **104**, 311.

THEODORSEN, T. 1952 Mechanism of turbulence. In *Proc. 2nd Midwestern Conf. on Fluid Mech. Ohio State University, Columbus, Ohio.*

TOWNSEND, A. A. 1970 Entrainment and the structure of turbulent flow. *J. Fluid Mech.* **41**, 13.